

# Trends in large-deformation analysis of landslide mass movements with particular emphasis on the material point method

K. SOGA\*, E. ALONSO†, A. YERRO†, K. KUMAR\* and S. BANDARA\*

Traditional geotechnical analyses for landslides involve failure prediction (i.e. onset of failure) and the design of structures that can safely withstand the applied loads. The analyses provide limited information on the post-failure behaviour. Modern numerical methods are able to simulate large mass movements and there is an opportunity to utilise such methods to evaluate the risks of catastrophic damage if a landslide occurs. In this paper, various large-deformation analysis methods are introduced and their applicability for solving landslide problems is discussed. Since catastrophic landslides often involve seepage forces, consideration of the coupled behaviour of soil and pore fluid is essential. Two approaches to model soil–pore fluid coupling in large-deformation analysis using the material point method (MPM) are introduced. An example simulation is presented for each approach; one on a model levee failure and the other on a natural cut slope failure (the Selborne experiment conducted by Cooper and co-workers in 1998). In the levee failure case, MPM simulation was able to capture a complex failure mechanism including the development of successive shear bands. The simulation was also able to predict excess pore pressure generation during the failure propagation and the subsequent consolidation stage. The simulations demonstrated the importance of the dilation characteristics of soil as well as changes in geometry for the post-failure behaviour. In the Selborne case, MPM was able to simulate the progressive failure of brittle, overconsolidated clay. The evolution of shear stresses along the failure surface was also captured by the MPM. The changes in the pore pressure and the actual shape of the failure surface were simulated by the MPM. The importance of accurately modelling the shear band within the MPM framework is highlighted.

KEYWORDS: landslides; numerical modelling

## INTRODUCTION

In nature, instabilities of slopes can manifest themselves in dramatic events involving sudden release of a large mass of soil, causing landslides. Among different types of landslides, the flow type slides (Hung *et al.*, 2001) such as sand/clay flow slides, debris flows and debris/rock avalanches can be very dangerous due to their rapid velocities and long run-out distances. The prediction of such catastrophic events presents several challenges and understanding the mechanics is of particular importance for risk assessment. Most geotechnical analyses involve failure prediction (i.e. onset of failure) and the design of structures that can safely withstand the applied loads. Although the probability of failure at the initiation stage of a landslide is often small, it is important to understand the post-failure behaviour so that the risk of catastrophic damage can be minimised. Hence there is a need to develop solution schemes that are capable of simulating failure initiation as well as post-failure dynamics of landslides.

The dynamics of a landslide involve at least three distinct scales: (a) the microscopic scale, which is characterised by the contact between grains; (b) the meso-scale, which represents microstructural effects such as grain rearrangement; and (c) the macroscopic scale, in which soil layering, faults and any other geological/geomorphologic features are important. For example, the flow of submarine landslides, which can be as much as 100 000 km<sup>3</sup> in volume, is influenced by the grain–

grain interactions and the hydrodynamics happening at the scale of a few micrometres to millimetres.

Typically continuum laws are only used when there is a strong separation of scales between the micro-scale and the macro-scale sizes of the landslide geometry. This paper provides an overview of continuum-based large-deformation analysis to simulate post-failure behaviour of landslides. Although continuum methods are useful in engineering design and interpretation, the grain level description of the granular material enriches the macro-scale variables that happen to account poorly for the local rheology of the materials. Numerical tools such as the discrete-element method (DEM) make it possible to evaluate quantities that are not accessible experimentally, thus providing useful insight into the flow dynamics. Grain–fluid interactions can be simulated by interfacing DEMs with a lattice Boltzmann solver or a computational fluid dynamics solver (He & Luo, 1997a, 1997b; Tsuji *et al.*, 2007; Kumar *et al.*, 2012; Capecelatro & Desjardins, 2013; Xiong *et al.*, 2014). However, these methods have their inherent limitations. Although millions of grains can be simulated, the possible size of such a grain system is generally too small to regard as ‘macroscopic’. Therefore, methods to perform a micro–macro transition are important and these ‘microscopic’ simulations of a small sample, that is, the ‘representative volume element’, can be used to derive macroscopic theories that describe the material within the continuum framework. This is an important research topic in its own right; however, it is beyond the scope of this paper.

Landslides and failure of slopes are caused by changes in the effective stresses, variation of material properties or changes in the geometry. Although the failure of geomaterials invariably refers to the attainment of a limit state, it is also possible to have material and spatial instability that

Manuscript received 11 March 2015; revised manuscript accepted 26 August 2015. Published online ahead of print 20 November 2015. Discussion on this paper closes on 1 August 2016, for further details see p. ii.

\* Department of Engineering, University of Cambridge, Cambridge, UK.

† Polytechnic University of Catalonia, Barcelona, Spain.

result in deformation modes with and without sharp discontinuities (Nicot & Darve, 2011). Two material failure modes are of interest when considering geomaterials: localised and diffuse failure modes (Darve *et al.*, 2004). At a material scale, the localised failure mode corresponds to a transition from a homogeneous strain pattern to a discontinuous one, characterised by the appearance of shear bands in which strains concentrate (Darve & Laouafa, 2000). On the contrary, the diffuse failure mode corresponds to a homogeneous occurrence of failure (Daouadji *et al.*, 2010). No visible pattern of localisation exists. A chaotic kinematic field dominates. Unlike shear bands, diffuse instabilities occur under fairly homogeneous deformation modes and drained instabilities are not generated by the excess pore pressures (Ramos *et al.*, 2012). This type of failure is usually observed in loose soils on gentle slopes. Further work is required to identify grain-scale behaviour that initiates a localised or a diffuse failure mode.

### NUMERICAL TECHNIQUES FOR MODELLING LARGE-DEFORMATION PROBLEMS

Table 1 lists various numerical methods available to solve large soil deformation problems. The basic features along with possible drawbacks are described for each method. Selected references are given to provide examples of how each method is used for landslide problems. It should be noted that the purpose of the table is not to give an authoritative view of the numerical techniques for modelling large-deformation problems (landslides in particular). It is to provide a point of reference for the readers to study further.

Conventional mesh-based Lagrangian approaches, such as the finite-element method (FEM) or the finite-difference method (FDM), are capable of modelling history-dependent material behaviour and have well-defined free surfaces. However, they require complex re-meshing and remapping of variables, causing additional errors in simulating large-deformation problems (Li & Liu, 2002). Unlike Lagrangian FEM, the computational mesh in Eulerian FEM is kept spatially fixed while the material is deforming in time. The Eulerian description produces the capability for handling large deformations without the problem of mesh distortion. As the computational mesh is completely decoupled from the material, convective terms appearing in the Eulerian FEM introduce numerical difficulties because of their non-symmetrical properties (Donea *et al.*, 1982). Additionally, Eulerian FEM is difficult to use with history-dependent constitutive models, which are commonly adopted to represent the mechanical behaviour of soils.

The coupled Eulerian–Lagrangian (CEL) method is an arbitrary Lagrangian–Eulerian method that attempts to capture the advantages of both the Lagrangian method and the Eulerian method in modelling large-deformation problems in geomechanics (Qiu *et al.*, 2011). For general geotechnical problems, a Lagrangian mesh is used to discretise structures, while an Eulerian mesh is used to discretise the subsoil. The interface between structure and subsoil can be represented using the boundary of the Lagrangian domain. On the other hand, the Eulerian mesh, which represents the soil that may experience large deformations, has no problems regarding mesh and element distortions. However, this requires greater computational time.

The element-free Galerkin (EFG) method is a mesh-less method, in which trial functions for the weak form are constructed using the moving least-squares interpolation (Belytschko *et al.*, 1994). The particle finite-element method (PFEM) is another mesh-less technique in which the nodal points represent the particles and the computational mesh is constructed by connecting these points. The mesh is then

used to solve the governing equations in a Lagrangian fashion, but large deformation requires frequent re-meshing (Kafaji, 2013).

In the case of flow slides, the run-out distances are up to two orders of magnitude greater than the length of the source of the landslide. The finite-element method with Lagrangian integration points (FEM-LIP) is a framework that is based on FEM analysis with material points travelling through the finite-element mesh. Moresi *et al.* (2003) derived the FEM-LIP scheme from the material point method but it is based on a fast-implicit solution method. It includes various particle-reweighting steps, which improve accuracy in the fluid deformation limit. In FEM-LIP formulation, the material points coincide with quadrature, which therefore move with respect to the mesh. The locations of the quadrature points are fixed for each element, and it is necessary to vary the weights in order to obtain the correct integral for a given element.

Smooth particle hydrodynamics (SPH) is the oldest mesh-free technique, in which the domain is discretised into particles that have a spatial distance referred to as the smoothing length, over which the material properties are ‘smoothed’ by a kernel function. SPH was developed to solve astrophysical problems (Monaghan, 2005). SPH has been applied in geomechanics for solving large-deformation problems (Mori, 2008; Augarde & Heaney, 2009; Maeda & Sakai, 2010). Although SPH has been successfully used in the past, it has a few drawbacks. SPH exhibits spatial instabilities, because of the point-wise integration (Bonet & Kulasegaram, 2000). Insufficient neighbouring particles potentially cause inconsistencies, and the boundary treatment is complex. It is computationally expensive as a result of the search for the neighbouring particles (Bandara, 2013).

The material point method (MPM) (Sulsky *et al.*, 1994, 1995) is a particle-based method that represents the material as a collection of material points, and Newton’s laws of motion determine their deformations. Sulsky *et al.* (1994) extended the particle-in-cell (PIC) method (Harlow, 1964) to computational solid mechanics by taking advantage of the combined Eulerian–Lagrangian approach. The MPM is a hybrid Eulerian–Lagrangian approach, which uses moving material points and computational nodes on a background mesh.

In this paper, the MPM is introduced as the authors’ preferred method for modelling landslide problems. The main reasons for this are as follows: (a) it can be used with large-scale failure analysis that undergoes large deformations since this method is based on continuum description of material flow using an Eulerian–Lagrangian approach; (b) the implementation is intuitive for users of FEM; (c) it can incorporate advanced history-dependent soil constitutive models; and (d) its application of boundary conditions is more straightforward than other mesh-free methods, such as the SPH method, owing to the presence of the background grid. Although it can be argued that other mesh-free methods have similar features, the main aim of the paper is to show that a mesh-free method is useful in simulating the complex mechanics of landslide motion during the failure, propagation and deposition stages.

### MATERIAL POINT METHOD (MPM)

#### General

The MPM is effective particularly in the context of large-deformation problems (Zhang *et al.*, 2009; Andersen & Andersen, 2010; Mackenzie-Helnwein *et al.*, 2010; Shin, 2010; Bandara, 2013; Mast *et al.*, 2014). Although not derived directly from what are classically considered as mesh-free or mesh-less methods, MPM is still regarded as a

mesh-free approach, primarily because the initial discretisation of the material does not involve a polygonal tessellation, as in the FEM. However, MPM utilises a background mesh to perform differentiation and integration, and to solve equations of motion (Steffen *et al.*, 2008). The background mesh can be of any form, although for computational efficiency a Cartesian lattice is adopted.

A typical two-dimensional (2D) discretisation of a solid body is shown in Fig. 1. The grey circles in the figure are the material points  $x_p$ , where  $p$  represents a material point, and the computational nodes are the points of intersection of the grid (denoted as  $X_i$ , where  $i$  represents a computational node). MPM involves discretising the domain,  $\Omega$ , with a set of material points. The material points are assigned with an initial value of position, velocity, mass, volume and stress, denoted as  $x_p$ ,  $v_p$ ,  $m_p$ ,  $V_p$  and  $\sigma_p$ , respectively. Depending on the material being simulated, additional parameters, such as pressure, temperature, pore-water pressure, and so on, are specified at the material points. The material points are assumed to be within the computational grid, as shown in Fig. 2. At every time step  $t_k$ , the MPM computation cycle involves projecting the data, such as position, mass and velocity, from the material points to the computational grid using the standard nodal basis functions, called the shape functions, derived from the position of the particle with respect to the grid. Gradient terms are calculated on the computational grid, and the governing equations, that is, the equations of motion, are solved with the updated position and velocity values mapping back to the material points. The mesh is re-initialised to its original state and the computational cycle is repeated.

One of the advantages of the MPM is that it can utilise history-dependent constitutive models. Since landslides may result in extensive shearing of soils, it is important to select an appropriate soil model that captures the critical state as well as the residual state. Furthermore, a user may wish to change the constitutive model during the course of simulation. For example, if the landslide mass comprises debris and there exists an established channel of water, it will result in an increase in water content during the flow (i.e. debris flow). This type of flow is usually modelled as a laminar single-phase fluid using Coulomb–Bingham rheology.

#### *The MPM for soil–water coupled problems*

The presence of pore water makes prediction of landslide behaviour a difficult task. During landslide mass movements, the resulting pore water pressure with different material types leads to different types of failure and post-failure stages. In particular, a landslide that involves loose, granular soil can experience excess pore pressure development and result in hazardous flow-slides, especially in natural and artificial cut/fill slopes associated with pyroclastic deposits, in situ weathered soils, loess deposits, mine tailings and waste deposits (e.g. Italy, Cascini *et al.*, 2008; the Alpine region, Mueller & Loew, 2009; China, Xu *et al.*, 2012). Analysis of these types of landslides requires a fully coupled hydromechanical framework to capture the initial acceleration phase of the post-failure stage. The change in pore water pressure by seepage or shear-induced contraction of the soil will change the shear resistance of the soil, which in turn can initiate landslides. The subsequent movement is also influenced by shearing characteristics of the soil and the development of pore water pressure.

Advanced numerical models based on MPM have been recently derived to capture the fully coupled dynamic behaviour in saturated soils during the failure and the post-failure stages (Zabala & Alonso, 2011; Abe *et al.*, 2013; Jassim *et al.*, 2013; Bandara & Soga, 2015). MPM can be used to model

the coupled hydromechanical behaviour during landslide mass movements if its governing equations are based on a fully coupled hydromechanical framework with advanced constitutive laws.

Recent developments in the MPM formulations that capture the fully coupled behaviour can be categorised into two main groups (see Fig. 3): (a) single material point layer to represent fully saturated soil and (b) two material point layers to represent fully saturated soil. Table 2 lists some of the references for each category and discusses their main features. An explicit time integration scheme has been used in all of these studies to predict the dynamic response of saturated soil. However, an implicit time integration scheme has been adopted by Beuth *et al.* (2008, 2010) to study large-deformation analysis using the quasi-static MPM.

In the first category (Fig. 3(a)), each material point contains information on both the soil and the pore fluid pressure (this can also be extended to include both air and water, see Yerro *et al.* (2015)). In this approach, the solid skeleton is represented in the Lagrangian formulation using material coordinates and the water phase is represented in the Eulerian formulation using the spatial coordinates (mass of water is not conserved). Most studies on the two-phase formulation neglect the relative acceleration of water with respect to the solid skeleton and consider the  $u$ – $p$  formulation for the governing equations with the generalised Darcy's equation (Zhang *et al.*, 2009; Higo *et al.*, 2010; Zabala & Alonso, 2011). This approach is required, as the Eulerian description is used to describe the water phase, which is limited to compute only the relative velocity of water with respect to the solid skeleton without storing its true velocity and updating its location.

Zhang *et al.* (2013) and Zheng *et al.* (2013) solved the momentum balance equation of the soil–water mixture as well as Darcy's equation in the background grid nodes in order to compute the pressure increments at material point locations using the mass balance equation of water. Zabala & Alonso (2011) obtained solutions for the solid acceleration and the pressure increment at the background grid nodes and computed the Darcy's velocity at the material point locations. In contrast, Jassim *et al.* (2013) considered the velocity formulation (i.e.  $u$ – $U$  formulation) and solved for solid and water accelerations at the grid nodes while using a single material point to carry both solid and water velocities. Higo *et al.* (2010) adopted a different approach in which they coupled the MPM with the FDM in order to separate the calculation of pore water pressures using a continuity equation at background cell centres by the FDM. Higo *et al.* (2010) extended the above approach to model unsaturated soil behaviour using a coupled MPM–FDM approach. Yerro *et al.* (2015) recently extended the single layer MPM approach to model unsaturated soils. It uses a three-phase approach that considers the mechanical behaviour of a solid skeleton and flow behaviour of water and air. This method was then applied to simulate the instability behaviour of a slope subjected to rainfall infiltration.

When a single layer of Lagrangian material points is considered, it only conserves the mass of the solid skeleton and does not guarantee the mass conservation of water. Also, most previous studies do not consider the relative acceleration of water with respect to the solid skeleton. Hence, it may not be suitable for application in high-frequency problems that involve rapid deformations.

In the second category (Fig. 3(b)), the coupled MPM formulations utilise two sets of Lagrangian material point layers to consider solid and water layers. The formulation has the advantage of conserving both solid mass and water mass. Shin (2010) and Mackenzie-Helnwein *et al.* (2010) used this approach to model solid–fluid mixtures with the MPM,

**Table 1. A summary of numerical methods to simulate landslide problems**

Methods	Examples/references	Description
<i>Continuum approaches</i>		
Mesh-based approaches		
Finite-element method (FEM)	<p>Cascini <i>et al.</i> (2013) used a hydro-mechanical FEM analysis to study the failure scenarios of a loose slope subjected to vertical downward water seepage.</p> <p>Eichenberger <i>et al.</i> (2013) numerically modelled the onset of failure of a rainfall-induced landslide in a steep slope composed of silty sand deposits using a fully coupled FE analysis with the ACMEG soil model.</p> <p>François <i>et al.</i> (2007) modelled large slope movements under unsaturated conditions by combining a hydrogeological model with a geomechanics model (pressure field calculated from the former model were used as input for the latter).</p> <p>Some more examples of application of FEM for landslide analysis include Sanavia (2009) and Cascini &amp; Cuomo (2010).</p>	<p>FEM involves discretisation of the mathematical model into disjoint (non-overlapping) components of simple geometry called finite elements.</p> <p>The response of each element is expressed in terms of a finite number of degrees of freedom characterised as the value of an unknown function, or functions, at a set of nodal points.</p> <p><i>Advantages</i></p> <ul style="list-style-type: none"> <li>• A hydromechanical FE analysis allows prediction of failure behaviour due to changes in fluid flow conditions.</li> </ul> <p><i>Drawbacks</i></p> <ul style="list-style-type: none"> <li>• Mesh distortion in large-deformation problems.</li> <li>• Complex re-meshing and remapping of variables cause additional errors in simulating large-deformation problems.</li> <li>• Not effective for post-failure behaviour.</li> </ul>
Finite-difference method (FDM)	<p>Guglielmi &amp; Cappa (2010) studied the gravitational movements of shallow rock over time using a three-dimensional finite-difference model generated from the regional digital elevation model. An element size of 50 m was adopted.</p> <p>Jiang <i>et al.</i> (2010) used the finite-difference technique to model large deformation failure due to draw-down of the Three Gorges reservoir in China. The Mohr–Coulomb model with matric suction was used to simulate unsaturated soil. The fluid–solid coupling is achieved by performing seepage calculation using porous media, while the mechanical soil skeleton is modelled using the Mohr–Coulomb criterion.</p> <p>Some more examples of use of finite difference in modelling landslides and debris flows include Chemenda <i>et al.</i> (2009); Shrestha <i>et al.</i> (2011); Lenti &amp; Martino (2013); and Rodriguez <i>et al.</i> (2013).</p>	<p>Derivatives in the partial differential equation are approximated by linear combinations of function values at the grid points. The domain is partitioned in space and in time and approximations of the solution are computed at the space or time points.</p> <p><i>Applications</i></p> <ul style="list-style-type: none"> <li>• Capable of simulating large deformation problems by updating the coordinates of the grid, but is restricted by the constitutive formulation.</li> <li>• Used for analysing simple geometries.</li> </ul> <p><i>Drawbacks</i></p> <ul style="list-style-type: none"> <li>• Restricted to prismatic elements in the mesh. Modelling complex geometries is difficult.</li> <li>• Mesh distortion causes issues in large deformation problems.</li> <li>• Requires greater computational time.</li> </ul>

*Continued*

Table 1 Continued

Methods	Examples/references	Description
Arbitrary Lagrangian Eulerian (ALE)	<p>Di <i>et al.</i> (2007) used the operator-split ALE technique to study the seismic response of a saturated slope using a non-linear elastoplastic model. The operator-split ALE involves two stages: (a) Lagrangian step, where the governing equations for the saturated soil, the equilibrium equation and the continuity equation are solved by the traditional, updated Lagrangian method, and (b) the Eulerian step, which involves mesh smoothing and transfer of state variables.</p> <p>Many researchers have applied the ALE technique to solve geotechnical problems, which involve large deformations, such as a rough footing on an undrained soil layer (Nazem <i>et al.</i>, 2009), consolidation problem (Nazem <i>et al.</i>, 2008) and soil–pipeline interactions (Fredj &amp; Dinovitzer, 2010). Kardani <i>et al.</i> (2011) implemented a refined h-adaptive finite-element technique in ALE to improve the numerical accuracy by continuously refining the mesh in the zone of concern.</p> <p>Detailed description of ALE can be found in Donea <i>et al.</i> (2004).</p>	<p>ALE combines the best features of both the Lagrangian and the Eulerian approaches. In the ALE description, the nodes of the computational mesh may be moved with the continuum in normal Lagrangian fashion, or be held fixed in an Eulerian manner, or be moved in some arbitrary specified way to give a continuous rezoning capability. The mesh follows the boundary.</p> <p><i>Advantages</i></p> <ul style="list-style-type: none"> <li>ALE offers freedom in moving the computational mesh, which allows for greater distortions of the continuum than would be allowed by a purely Lagrangian method, and with more resolution than that offered by a purely Eulerian approach.</li> </ul> <p><i>Drawbacks</i></p> <ul style="list-style-type: none"> <li>The freedom in mesh movement has its limits and mesh tangling is still observed for large deformation problems.</li> <li>Necessity of a convective step to displace nodes based on the contact algorithm. The convective effect has to be taken in to account for history-dependent variables.</li> <li>Although pure Lagrangian boundary conditions avoid the convective algorithm, this method results in mesh distortion and non-convexity in the global mesh.</li> </ul>
Coupled Eulerian – Lagrangian (CEL)	<p>Qiu <i>et al.</i> (2011) used the CEL method to capture the behaviour of strip footing on a Drucker–Prager elasto-plastic model and a pile-jacking problem. The Eulerian soil material is tracked as it flows through the mesh by computing its Eulerian volume fraction (EVF). Each Eulerian element is designated a percentage, which represents the portion of that element filled with soil. If an Eulerian element is completely filled with soil, its EVF is 1; if there is no soil in the element, its EVF is 0. Contact between Eulerian materials and Lagrangian materials is enforced using a general contact that is based on a penalty contact method. The Lagrangian elements can move through the Eulerian mesh without resistance until they encounter an Eulerian element filled with material (EVF &gt; 0).</p> <p>Brown <i>et al.</i> (2002) present different contact algorithms that have been proposed to model the interaction between the Eulerian and the Lagrangian materials.</p> <p>Guilkey <i>et al.</i> (2003) and Harman <i>et al.</i> (2003) used CEL for large-deformation fluid–structure interaction problems.</p>	<p>The CEL method also attempts to capture the strengths of the Lagrangian and Eulerian methods. In general, a Lagrangian frame is used to discretise the moving structure while an Eulerian frame is used to discretise the fluid domain. The boundary of the Lagrangian domain is taken to represent the interface between the different domains. Interface models use the velocity of the Lagrangian boundary as a kinematic constraint in the Eulerian calculation and the stress from the Eulerian cell to calculate the resulting surface stress on the Lagrangian domain.</p> <p><i>Advantages</i></p> <ul style="list-style-type: none"> <li>Effective for modelling fluid–solid interactions.</li> </ul> <p>The free deformable soil in an Eulerian domain overcomes the impacts of the singular plasticity points near the interfaces automatically.</p> <p><i>Drawbacks</i></p> <ul style="list-style-type: none"> <li>Requires additional advection terms to handle the transport of quantities related to the mesh.</li> <li>Requires greater computational time.</li> <li>Numerical solution depends on the coarseness of the Eulerian mesh.</li> </ul>

Continued

Table 1 Continued

Methods	Examples/references	Description
Mesh-free techniques Material point method (MPM)	<p>Jassim <i>et al.</i> (2013) applied the MPM to solve quasi-static problems such as pile driving. Zabala &amp; Alonso (2011) studied the progressive failure of a dam using a strain-softening elasto-plastic model in MPM. Beuth <i>et al.</i> (2008, 2010) used an implicit time integration scheme to study large-deformation problems using quasi-static MPM.</p> <p>MPM is extended to solve coupled hydromechanical problems of fluid-saturated soil subjected to large deformation using Biot's mixture theory. Separate material points for the fluid are used to simulate the seepage of water through the porous soil skeleton (Abe <i>et al.</i>, 2013; Bandara &amp; Soga, 2015).</p> <p>Higo <i>et al.</i> (2010) used coupled MPM with FDM to study seepage response of saturated and partially saturated soils. Governing equations for the soil skeleton and the pore fluid are discretised by the MPM and FDM, respectively.</p>	<p>A hybrid Eulerian–Lagrangian approach, which uses moving material points and computational nodes on a background mesh. The body is represented as a collection of material points, and Newton's laws of motion determine their deformations.</p> <p><i>Advantages</i></p> <ul style="list-style-type: none"> <li>• Ability to simulate large-deformation problems without mesh distortion problems.</li> <li>• Simulate fluid–solid interactions in large-deformation problems.</li> </ul> <p><i>Drawbacks</i></p> <ul style="list-style-type: none"> <li>• Use of linear shape functions in large-deformation problems causes numerical errors due to material points crossing grids called the cell crossing noise.</li> <li>• Higher dimensional shape functions require greater computational time.</li> <li>• Computational cost is higher than FEM.</li> </ul>
Smooth particle hydrodynamics (SPH)	<p>Blanc &amp; Pastor (2012) proposed a stabilised fractional step, Runge–Kutta Taylor SPH algorithm to model coupled behaviour in saturated soil that can avoid instabilities and oscillations of pore pressure in general SPH coupled formulations.</p> <p>Mori (2008) applied two-phase SPH to river levee failure analysis. Maeda &amp; Sakai (2010) represented the solid phase, liquid phase and the gas phase as separate layers of SPH particles to simulate seepage-induced failures around sheet piles and dykes.</p> <p>Bui <i>et al.</i> (2008) performed collapse of a granular column and bearing capacity failure problem using SPH with an elasto-plastic model.</p> <p>Further examples of application of SPH to landslide modelling include Basu <i>et al.</i> (2011); Cascini <i>et al.</i> (2014); Pastor <i>et al.</i> (2009, 2014).</p>	<p>The domain is discretised into particles that have a spatial distance, called the smoothing length, over which the material properties are 'smoothed' by a kernel function.</p> <p><i>Applications</i></p> <ul style="list-style-type: none"> <li>• Simulation of large-deformation problems.</li> <li>• Modelling fluid flow in large-deformation problems.</li> </ul> <p><i>Drawbacks</i></p> <ul style="list-style-type: none"> <li>• Requires special boundary treatment approaches, such as use of ghost nodes.</li> <li>• SPH exhibits spatial instabilities, as a consequence of the pointwise integration.</li> <li>• Insufficient neighbouring particles cause inconsistencies.</li> <li>• Computationally expensive as a result of the search for the neighbouring particles.</li> <li>• Suffers from tensile instability, which causes numerical fracture.</li> </ul>
Particle finite-element method (PFEM)	<p>Oñate <i>et al.</i> (2008) simulated surface erosion using PFEM by detaching elements belonging to the bed surface in terms of the frictional work at the surface originated by the shear stresses in the fluid.</p> <p>Zhang <i>et al.</i> (2015) employed two-dimensional plane-strain PFEM simulation to study whole procedure of the landslide, from initiation, sliding to deposition.</p> <p>Some more examples of use of PFEM in debris flows and landslide modelling include Zhang <i>et al.</i> (2015), Cremonesi &amp; Perego (2013) and Oñate <i>et al.</i> (2011).</p>	<p>The PFEM is a numerical method that uses a finite-element mesh to discretise the physical domain and to integrate the differential governing equations. The nodes of the mesh move according to the equations of motion in an updated Lagrangian fashion. The nodes transport their momentum together with all their physical properties, thus behaving as particles. At the end of each time step the mesh has to be rebuilt as the nodes have been moved to their new time step position. The Delaunay Tessellation is chosen to connect all the particles at the new time step position giving as a result a new mesh. The resulting mesh not only works as a support where the differential equations are integrated, it is also used to identify the contacts and to track the free surface.</p> <p><i>Applications</i></p> <ul style="list-style-type: none"> <li>• Large deformation problem with fluid–solid coupling.</li> <li>• Static and dynamic excavation problems.</li> <li>• Modelling free-surface evolution.</li> </ul> <p><i>Drawbacks</i></p> <ul style="list-style-type: none"> <li>• Contact between solid–solid nodes and solid–fluid nodes require special treatment.</li> <li>• Large deformation requires frequent re-meshing.</li> </ul>

Continued

Table 1 Continued

Methods	Examples/references	Description
Finite-element method with Lagrangian integration points (FEMLIP)	<p>Moresi <i>et al.</i> (2003) derived the FEMLIP scheme from the MPM, but it differs in a number of important aspects, including the fact that it is based on a fast-implicit solution method, and that it includes various particle-reweighting steps, which improve accuracy in the fluid-deformation limit.</p> <p>Cuomo <i>et al.</i> (2013) adopted the FEMLIP technique with an elastic–perfectly plastic material to model the effect of a vertical cut excavation in a soil deposit.</p> <p>Prime <i>et al.</i> (2014) use an elasto-plastic relation and a Bingham viscous law linked by a mechanical transition criterion to model landslides in the FEMLIP framework. A parametric study is performed to understand the influence of plastic and viscous parameters on the flow development and arrest.</p>	<p>FEMLIP is based on a kinematic dissociation between the material points and the computational nodes of the finite-element Eulerian mesh. For a given material configuration, the material points are used as integration points on one element. All material properties including the internal variables are stored at the material points and are accurately tracked during the advection process.</p> <p><i>Advantages</i></p> <ul style="list-style-type: none"> <li>• Ability to simulate extremely large deformation without significant change in accuracy; the ability to track material history and interfaces through time.</li> <li>• Faster computational algorithm.</li> </ul> <p><i>Drawbacks</i></p> <ul style="list-style-type: none"> <li>• Large material strains produce elongated ‘local volumes’ for particles. In order to maintain the representative volume of each particle, new particles are created. This results in a very high storage requirement.</li> <li>• The resolution is related to the grid point spacing, not the finer particle spacing.</li> </ul>
Element-free Galerkin (EFG)	<p>Kumar <i>et al.</i> (2008) used the EFG method to model unsaturated flow through a rigid porous medium with applications in contaminant transport modelling. They show that a higher degree of accuracy is available using this method as compared to conventional FE for similar number of degrees of freedom.</p> <p>Kim &amp; Inoue (2007) modelled 2D seepage flow through porous media using the basic EFG method with the addition of stochastic to model variable permeability in heterogeneous ground.</p>	<p>The EFG (Lu <i>et al.</i>, 1994) can be described in a similar fashion to FEMs using shape functions. For EFG, the shape functions are derived from a moving least-squares approach. Each node has a zone of ‘influence’, which is usually radially symmetric (in two dimensions, for instance). Typical weight functions used are truncated splines and exponentials, which are smooth and continuous. The weak form is local to each node. The test functions used are often the weight functions with a different radius of support. As long as all the local sub-domains overlap to cover the global domain, the global equilibrium and boundary conditions will be satisfied.</p> <p><i>Advantages</i></p> <ul style="list-style-type: none"> <li>• The dependent variable and its gradient are continuous in the entire domain.</li> </ul> <p><i>Drawbacks</i></p> <ul style="list-style-type: none"> <li>• Greater computational time.</li> <li>• EFG is not a true mesh-less method as the global integration requires the division of the domain into cells, which can be considered similar to the generation of a mesh.</li> </ul>

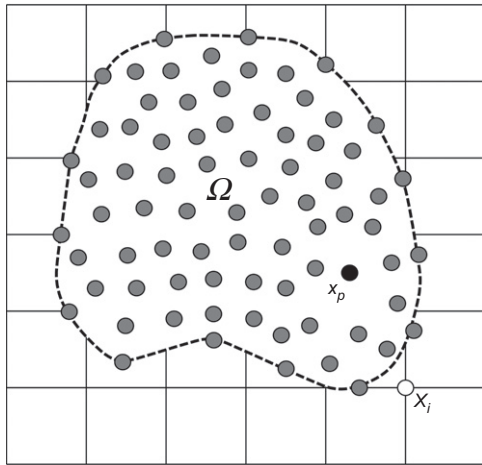


Fig. 1. Typical discretisation of a domain in MPM

which was derived based on the mixture theory approach. They considered the momentum balance equation for each phase along with drag interaction models to solve the acceleration of each phase in the Eulerian formulation. This approach requires drag interaction models to capture the interaction between phases through drag forces that occur due to the relative motion of the phases. This formulation is quite different from the soil mechanics based MPM formulations – it does not consider the mixture to be composed of a solid skeleton layer and seepage water layer.

Abe *et al.* (2013), Bandara (2013) and Bandara & Soga (2015) used the MPM to model saturated soil with a solid skeleton and pore water material point layers while using the effective stress approach to capture the solid skeleton behaviour. Abe *et al.* (2013) considered the Biot's mixture theory formulation while neglecting the relative acceleration of water with respect to the solid skeleton. This requires the velocity of the water phase to be computed at each time step using the generalised Darcy's equation, which may lead to limitations in modelling rapid motions. Bandara (2013) and Bandara & Soga (2015) derived a coupled MPM formulation based on the mixture theory approach considering the relative acceleration of water with respect to the solid skeleton. Fig. 3(b) shows a schematic diagram of the MPM approach with two sets of material point layers adopted by Bandara & Soga (2015). This method allows modelling of extremely rapid flows while also conserving the mass of both solid skeleton and pore water. Use of two material point layers is extremely helpful when modelling soil–water interaction problems such as submarine landslides, dredging and erosion modelling. For instance, it allows modelling of fluidisation of soil particles at the water interface and simulations of internal erosion by transferring a portion of soil particle mass to fluid particle. However, the existence of two layers of material points results in greater computation time, and careful modelling of interface regions that separate saturated soil from dry soil and free water is required.

#### A MODEL LEVEE FAILURE BY SOIL–WATER TWO-PHASE USING TWO-LAYER MPM

This section shows the applicability of MPM to model fully coupled dynamic problems that undergo large deformations in saturated soils using the mixture theory based formulation. As discussed earlier, the formulation considers two sets of Lagrangian material points to represent soil skeleton and pore water layers. Further details of the formulation can be found in Bandara & Soga (2015).

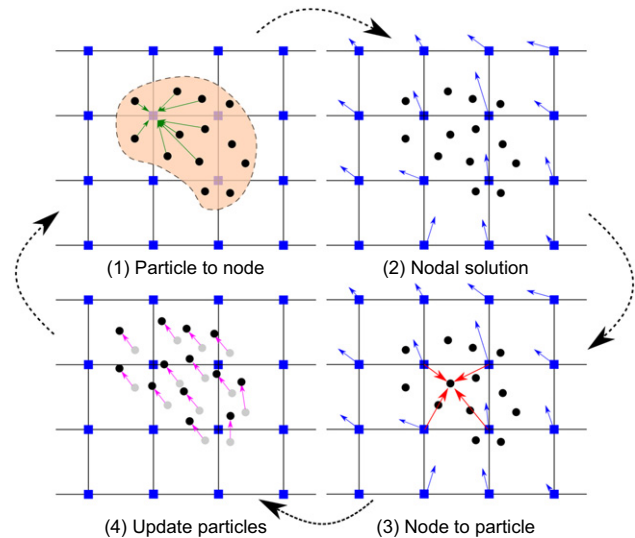


Fig. 2. Illustration of the MPM algorithm. (1) A representation of material points overlaid on a computational grid. Arrows represent material point state vectors (mass, volume, velocity, and so on) being projected to the nodes of the computational grid. (2) The equations of motion are solved on to the nodes, resulting in updated nodal velocities and positions. (3) The updated nodal kinematics is interpolated back to the material points. (4) The state of the material points is updated, and the computational grid is reset

A scenario of levee failure due to increased seepage is considered in order to show the capability of the MPM approach. This levee failure model closely resembles a large-scale experimental investigation on river levee failure, which was carried out by Iseno *et al.* (2004) and discussed in Abe *et al.* (2013) and Bandara (2013).

#### Levee model

The experimental procedure of the levee model involved inducing a seepage flow into an initially unsaturated river levee. A static water pressure was applied at the back of the model using a large water tank (Iseno *et al.*, 2004). The experimental configuration is shown in Fig. 4. The levee was composed of very loose, sandy soil with average degree of compaction of 75%, initial water content of 19.4%, initial saturation of 60% and permeability of  $4.5 \times 10^{-5}$  m/s. The water level at the upstream side of the model was raised to induce seepage failure. During the seepage flow, the levee remained stable for 13 h and 10 min, except for a small failure that took place 1.5 m from the toe of the model after 12 h and 30 min due to internal erosion. A complete progressive failure occurred afterwards for a duration of 30 s. The initial configuration for the numerical model is shown in Fig. 4(c), in which the phreatic surface just before the failure was considered to avoid long computational time. Just before the failure, the measured suction and saturation values slightly above the phreatic line were 2.7 kPa and 82%, respectively. These values were used as the initial conditions for the simulations.

#### The MPM model

As shown in Fig. 4(c), the region below the phreatic line contains two sets of material points to represent soil skeleton layer and pore water, and the region above the phreatic line contains only one material point layer that represents the soil skeleton. The unsaturated soil behaviour above the phreatic surface is modelled using a simple approach based on



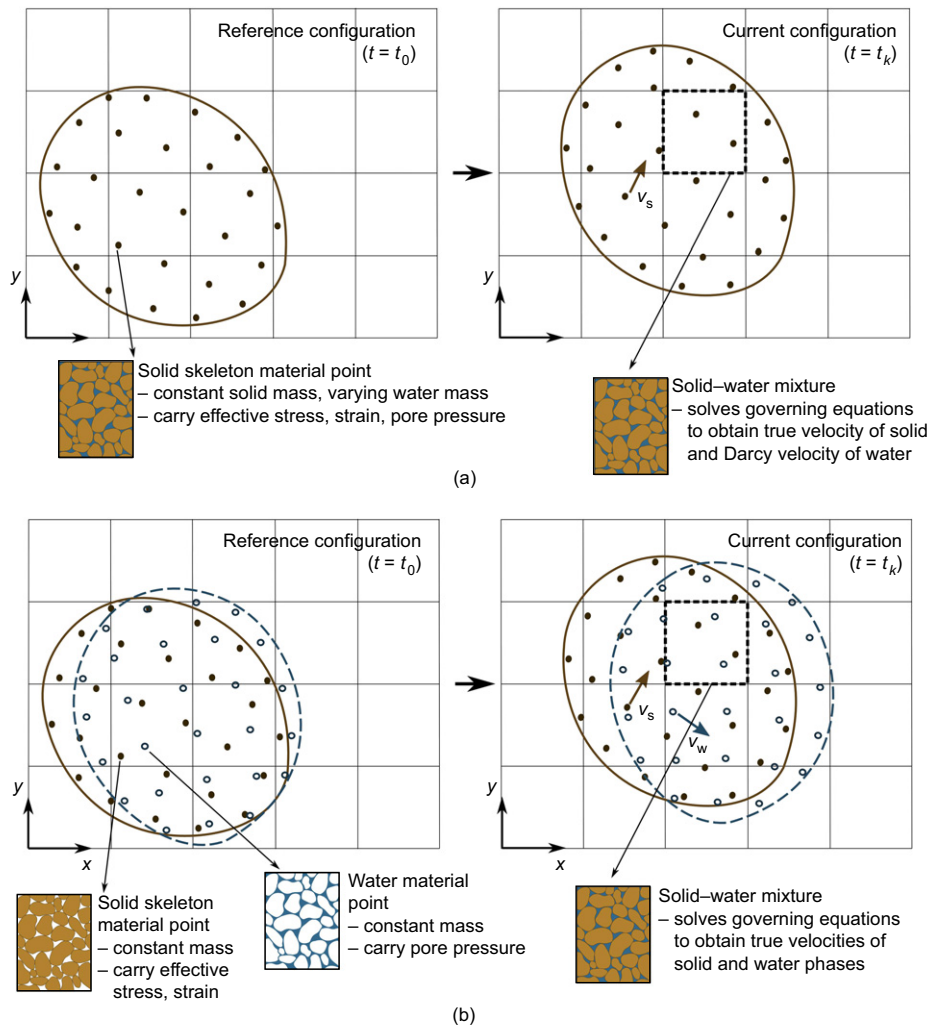


Fig. 3. Schematic diagram of the computational grid and material points for the coupled MPM with: (a) single layer of material points; (b) two layers of material points

Bishop's effective stress concept by considering: (a) increased mass due to water for a saturation of 82%; (b) an additional suction component of  $S_w s \mathbf{m}$  is added when solving the momentum balance equation of the mixture ( $S_w$  is the saturation ratio,  $s$  is the suction and  $\mathbf{m}$  is the Kronecker delta vector); and (c) capillary cohesion  $c'_{u, \text{mob}}$  in addition to  $c'$  are used to model the effect of suction-induced hardening.  $S_w$ ,  $s$  and  $c'_{u, \text{mob}}$  values of a solid material point are automatically set to zero when the background cell is occupied with a water material point. The initial values for the effective stress and the pore water pressure are computed from a preliminary static solution considering the initial configuration shown in Fig. 4(c). The numerical model contains 7200 soil material points and 4974 water material points initially distributed in a background grid of four material points per cell with 0.1 m cell length. The simulations were performed with a time step of  $1.0 \times 10^{-5}$  s. The bottom boundary is modelled using Coulomb's friction criterion (Bandara & Soga, 2015) considering a friction coefficient of 0.3. Bandara (2013) performed three simulations with different friction coefficients (0.2, 0.3 and 0.6) and found out that the failure behaviour becomes significantly different only when using a very small friction coefficient (i.e. 0.2).

#### Constitutive model

A non-associated Mohr–Coulomb model with simple strain-hardening/softening behaviour is adopted to capture

the effective stress behaviour of the solid skeleton. The mobilised values of effective friction angle  $\phi'$ , effective cohesion  $c'$  and dilation angle  $\Psi$  are obtained according to the value of total plastic deviatoric strain, as shown in Fig. 5.  $\gamma_{\text{dev, pl}}^{\text{peak}}$  represents the plastic deviatoric strain at peak, and  $\gamma_{\text{dev, pl}}^{\text{crit}}$  represents the plastic deviatoric strain when the softening or hardening is completed. The soil is modelled considering Young's modulus  $E = 1.0 \times 10^7$  Pa, Poisson ratio  $\nu = 0.3$ , solid grain density  $\rho_s = 2700 \text{ kg/m}^3$ , initial porosity  $\eta_0 = 0.46$ , initial permeability  $k_0 = 5.0 \times 10^{-4}$  m/s and effective cohesion  $c' = 0$  Pa. Three numerical simulations were performed considering three different peak dilation angles  $\psi_{\text{peak}} = 0^\circ, -1.0^\circ$  and  $5.0^\circ$  when the total plastic deviatoric strain  $\gamma_{\text{dev, pl}}$  was less than  $\gamma_{\text{dev, pl}}^{\text{peak}}$  of 0.01. These values change linearly with increasing  $\gamma_{\text{dev, pl}}$  and reach the critical state dilation angle of  $\psi_{\text{crit}} = 0$  when  $\gamma_{\text{dev, pl}}$  is equal to  $\gamma_{\text{dev, pl}}^{\text{crit}} = 0.2$ . All the simulations considered the peak value of capillary cohesion as 0.5 kPa, a capillary cohesion at critical state of 0 kPa, a peak friction angle of  $30.8^\circ$  and a critical state friction angle of  $30.8^\circ$ . Water was modelled with a density of  $1000 \text{ kg/m}^3$  and a bulk modulus of 1.0 GPa. These three simulations were selected to identify the capabilities of the MPM formulation and to understand the importance of the dilation characteristics of soil. However, the authors do not intend to capture the exact soil constitutive behaviour related to very loose sandy soil that was used in the experiment because of the limitations of the simple constitutive model adopted in the present study. The selection of an appropriate

**Table 2. Modelling of soil–pore water coupling using MPM**

Single material point layer to represent fully saturated soil	Zhang <i>et al.</i> (2009)	Developed to predict the dynamic responses of saturated soil subject to contact/impact, based on the $u$ – $p$ form governing equations. Fluid acceleration with respect to the soil skeleton ( $a_{ws}$ ) is neglected
	Zabala & Alonso (2011)	Coupled MPM formulation based on extended Biot's approach (Zienkiewicz <i>et al.</i> , 1984) while neglecting $a_{ws}$ , is used to simulate the construction and failure of the Aznalcollar dam. The brittle foundation clay is modelled as a strain-softening Mohr–Coulomb elasto-plastic model
	Jassim <i>et al.</i> (2013)	Coupled dynamic, two-phase MPM formulation by way of velocity formulation (i.e. consider both solid and fluid phase accelerations) with a single layer of material points. Applied to model the effect of wave attack on a sea dyke
	Zheng <i>et al.</i> (2013)	Same governing equations as in Zhang <i>et al.</i> (2009) but with improved convected particle domain interpolation method that reduces the numerical artefact noises due to material points crossing computational grid boundaries
	Higo <i>et al.</i> (2010)	Simple coupled MPM–FDM approach to model fluid saturated soil with elasto-plastic material model. MPM method is used to represent soil particles and the fluid is represented using an Eulerian approach with FDM
Single material point layer to represent unsaturated soil	Higo <i>et al.</i> (2015)	Simple coupled generalised interpolation material point (GIMP)–FDM to model partially saturated soil with elasto-plastic material model considering constant air pressure. GIMP method is used to represent soil particles and the fluid is represented using an Eulerian approach with FDM. Applied to model the dynamic deformation behaviour of unsaturated embankment due to seepage flow
	Yerro <i>et al.</i> (2015)	Coupled MPM approach to model partially saturated soil using three phases (i.e. solid, water, air). A suction-dependent elasto-plastic Mohr–Coulomb model, expressed in terms of net stress and suction variables, is implemented. This formulation is used to model the instability of a slope subjected to rain infiltration
Two material point layers to represent fully saturated soil	Mackenzie-Helnwein <i>et al.</i> (2010) and Shin (2010)	Modelled solid–fluid mixtures using MPM by representing solid (i.e. not as a solid skeleton as in soil mechanics) and fluid particles as Lagrangian particles using mixture theory approach
	Abe <i>et al.</i> (2013)	Modelled coupled hydromechanical problems in saturated soil using two layers of Lagrangian material points to represent solid skeleton layer and pore fluid layer based on Biot's mixture theory neglecting $a_{ws}$
	Bandara (2013) and Bandara & Soga (2015)	Modelled rapid failure behaviour in fully saturated soils based on mixture theory approach while using two sets of Lagrangian material point layers to represent solid skeleton and pore water while taking into account $a_{ws}$

constitutive model is the key to having successful simulations. Further work is needed to understand the contribution of the constitutive model on the overall behaviour of a landslide.

### Results

Figure 6 shows the contour plots of deviatoric shear strain, pore pressure and vertical effective stress for the simulations with three different dilation angles at peak after a time of 2.5 s. Different failure patterns can be identified from each simulation as a result of having different mobilised dilation angles during failure. The case with negative  $\psi_{\text{peak}}$  results in very large deformations due to high excess pore pressure development upon shearing and higher reductions in vertical effective stress compared to the case with zero  $\psi_{\text{peak}}$ . On the other hand, the case with positive  $\psi_{\text{peak}}$  shows only minor variations of pore water pressure and vertical effective stress, and the levee remains stable during the entire simulation except for a small localised failure at the toe area due to seepage flow.

Figure 7 shows some photographs that were taken during the experiment and it can be seen that the failure started from the toe and the levee failed in a progressive manner. Tensile-like cracking along the surface of the model is visible

throughout the failure. The final shape of the levee after the failure predicted by the zero dilation case is in good agreement with the experiment shown in Fig. 6(a). The differences in the failure behaviour in the simulation can be the result of: (a) not modelling the unsaturated soil behaviour above the phreatic surface accurately; (b) not modelling the entire seepage water front movement; and (c) not being able to capture the soil strength parameters that are dependent on density and mean pressure.

A large-deformation failure mechanism can be observed when using a negative  $\psi_{\text{peak}}$  that depicts a light contractile soil as shown in Fig. 6(b). A detailed failure description is shown in Fig. 8, which includes deviatoric shear strain, pore pressure and vertical effective stress profiles at different times during the failure. According to Fig. 8(a), a progressive type of failure can be observed as more shear bands develop with time and spread towards the levee. High excess pore pressures can be observed, especially in the regions of shear bands. At the same time, the effective vertical stresses also keep on reducing with time due to change in geometry. Once the deformations cease, the excess pore pressure dissipates and the vertical effective stress increases. The size of the shear band obtained from the adopted formulation can be dependent on the space discretisation because the present

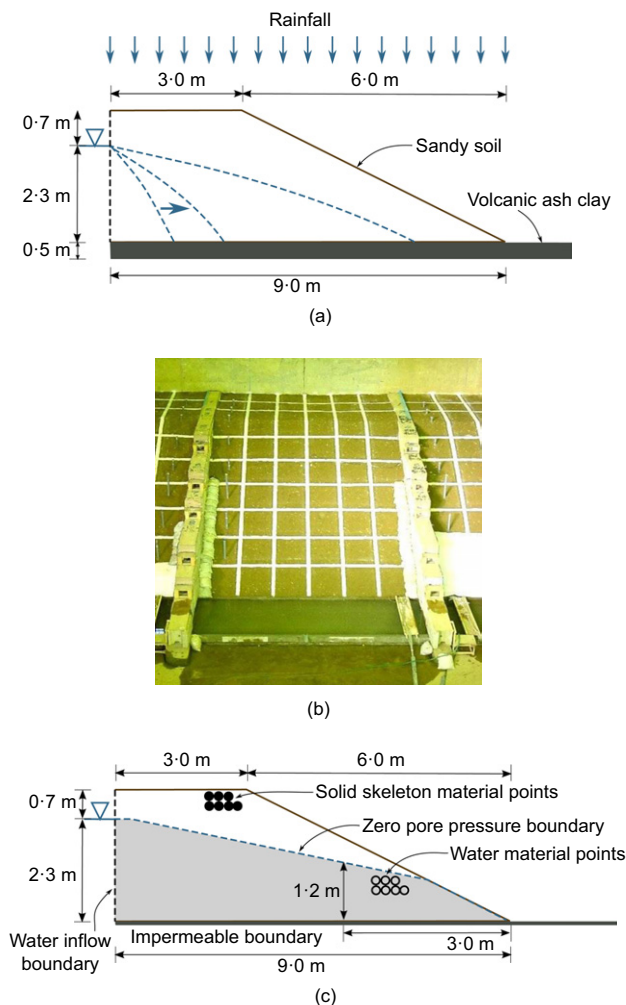


Fig. 4. Experimental and MPM model set-ups: (a) schematic diagram of the experimental configuration; (b) front view of the initial experimental set-up (Mori, 2008); (c) schematic diagram of the MPM model

formulation does not consider any regularisation technique to limit the mesh-dependent strain localisation.

#### Progressive failure

Different failure mechanisms can be observed for the levees between two cases with zero and negative dilation angle at peak as shown in Figs 9(a) and 9(b). The levee with zero dilation angle fails in a progressive failure pattern with one major shear band as shown in Fig. 9(a). However, for the case with  $\psi_{\text{peak}} = -1.0^\circ$ , a retrogressive type of failure pattern is visible due to successive development of shear bands during the failure and propagation. Primary shear bands are shown in Fig. 9(b). This behaviour can be further observed from Figs 8 and 9(c). According to Fig. 9(c), first the initial shear band develops from location P3 towards P5, and then successive shear bands are generated (deviatoric shear strain at point P2 increases after the failure of points P3, P4 and P5).

Figure 10 shows the motion paths of selected material points during the entire simulation time for the zero dilation case (Fig. 10(a)) and the negative dilation case (Fig. 10(b)). The levee with negative  $\psi_{\text{peak}}$  results in significant run-out distance. Fig. 11 shows a detailed comparison of velocity, displacement and total deviatoric shear strains at material points C1, C2, C3 and C4. The material points that are located above the initial shear band undergo very large

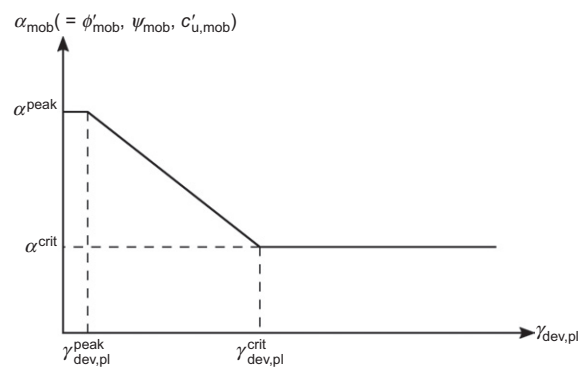


Fig. 5. Variation of mobilised friction angle, dilation angle and cohesion with plastic deviatoric shear strain for the Mohr-Coulomb model (Bandara, 2013)

displacements (see points C3 and C4). Most of the material points in this region tend to slide above the shearing material under relatively small shearing (see point C3 and Fig. 8(a)). Relatively higher velocity can be observed for sliding material than for material that is located in the primary shear bands (see point C3).

#### Behaviour at material points

A detailed comparison between the simulations with zero and the negative  $\psi_{\text{peak}}$  cases is shown in Fig. 12 considering the evolution of pore pressure, vertical effective stress and velocity at three different material point locations (i.e. P3 is located in the initial shear band in both simulations, P2 is located in a consecutive shear band in the simulation with the negative  $\psi_{\text{peak}}$ , and P1 is located in a position that does not undergo any shear deformations). The velocity plot with the negative  $\psi_{\text{peak}}$  case also contains the evolution of mobilised dilation angle for P1, P2 and P3.

In the case with negative  $\psi_{\text{peak}}$  (see Fig. 12(b)), when the initial shear band develops at P3, the pore pressure rises significantly (more than twice the initial pore pressure) due to the contractive tendency of the soil upon shearing. During this time the vertical effective stress also reduces by more than twice the initial value. The velocity increases rapidly (due to a sudden acceleration phase of soil). At P2, the peak pore pressure and minimum vertical effective stress occur after some delay as a result of the subsequent development of shear bands. The instability is a direct result of the presence of negative mobilised dilation angle at these points just before the rapid failure. The negative mobilised dilation angle along the shear bands creates a tendency for the solid skeleton to contract along the shearing regions. However, the rapid movement of the soil body causes the soil to be in the undrained condition, thus generating very high excess pore water pressures and reducing the effective stresses. The reduction in the mean effective stresses close to zero can result in instabilities in the soil, which is quite similar to the case of static liquefaction and instability in loose, granular soils that tend to contract upon shearing.

In the case with zero  $\psi_{\text{peak}}$  (see Fig. 12(a)), there is a more uniform change in the pore pressure and vertical effective stresses with time. The slight reductions in pore pressure are associated with the reduction of the water table height, and the changes in the vertical effective stress are due to the geometric changes in the height of the overburden.

The stress path  $p'-q$  of a material point that is located at the initial shear band is shown for each levee with  $\psi_{\text{peak}} = -1.0^\circ$  and  $\psi_{\text{peak}} = 0^\circ$  cases in Figs 13(a) and 13(b). Each figure contains a time history of  $p'$  and  $q$  values

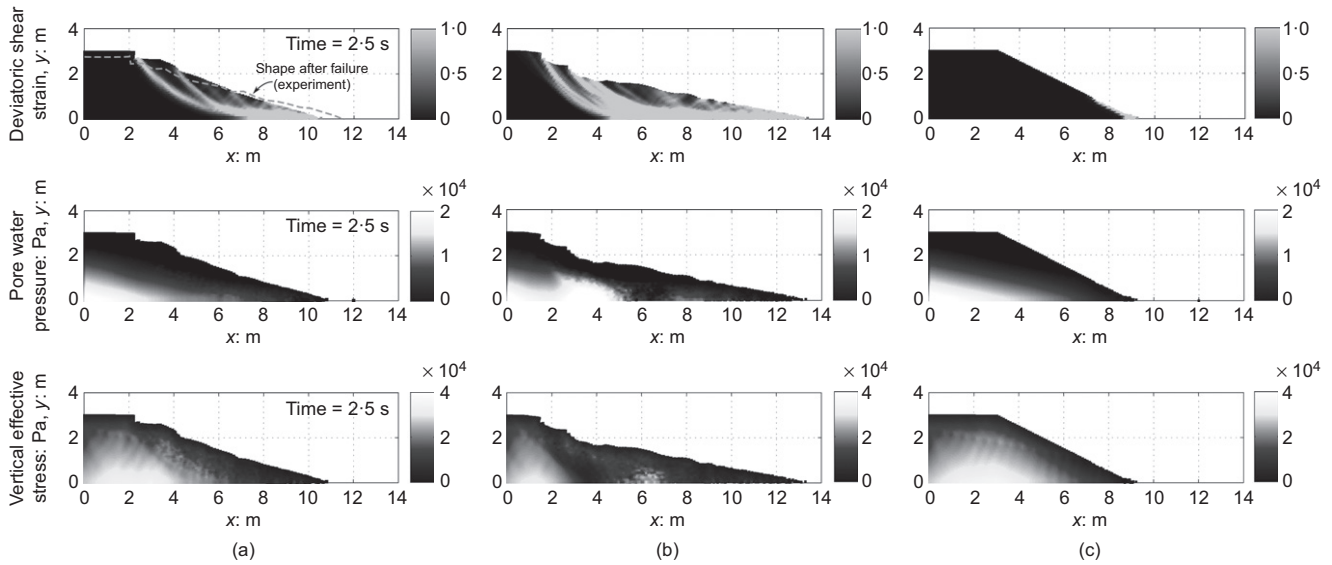


Fig. 6. Comparison of failure behaviour of levees with different dilation angles at peak: (a)  $\psi_{\text{peak}} = 0^\circ$ ; (b)  $\psi_{\text{peak}} = -1^\circ$ ; (c)  $\psi_{\text{peak}} = 5^\circ$

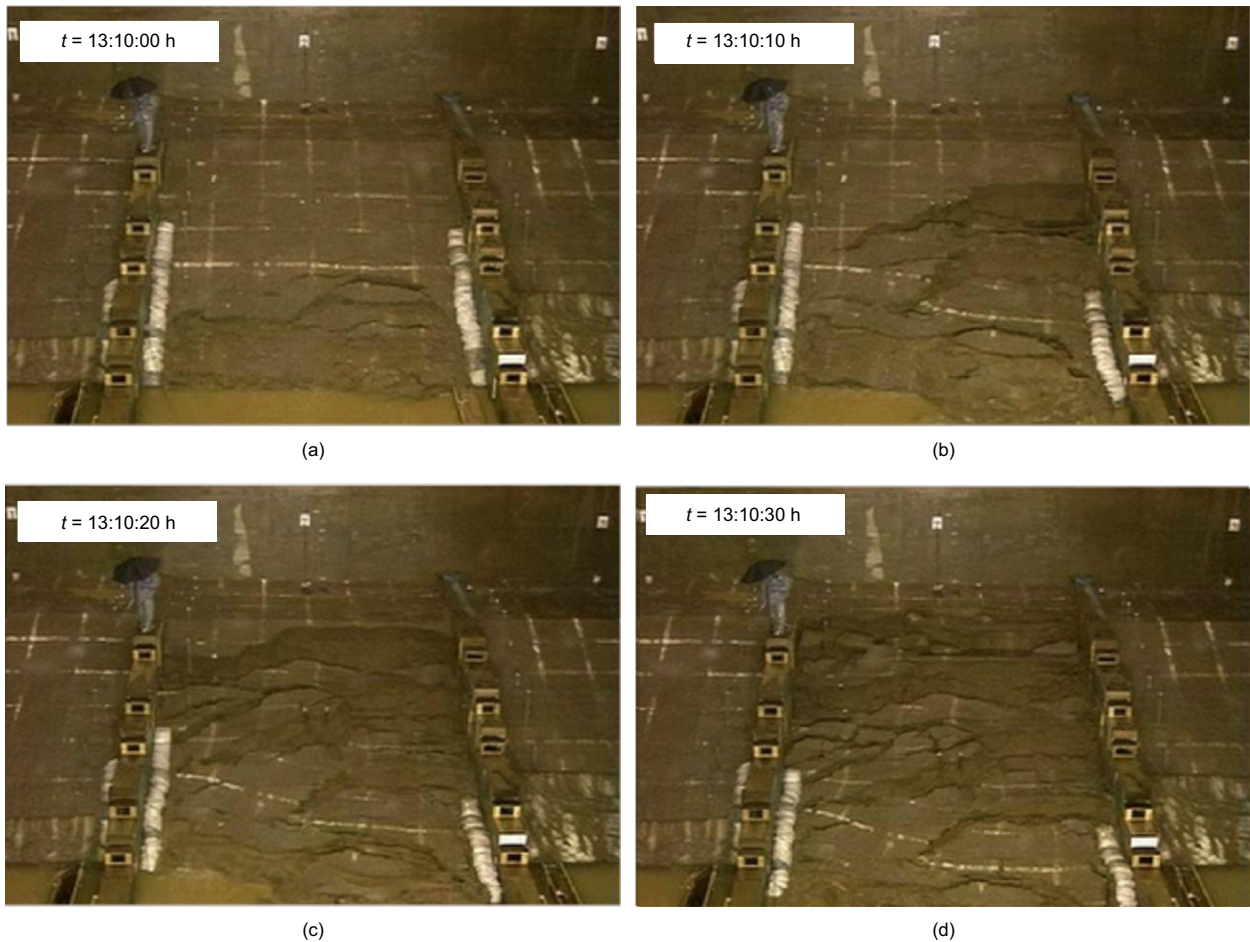


Fig. 7. Progressive failure evolution for the levee failure experiment with rainfall (Mori, 2008): (a) initial failure at toe; (b) initial stage of progressive failure; (c) intermediate stage of progressive failure; and (d) final failure profile of the levee

(A, B, C, D, E points are located at times 0 s, 0.25 s, 0.5 s, 1.25 s and 3.5 s).  $p'$ - $q$  space is calculated using effective mean stress  $p' = (\sigma'_1 + \sigma'_2 + \sigma'_3)/3$  and deviatoric stress  $q = 1/\sqrt{2} \sqrt{(\sigma'_1 - \sigma'_2)^2 + (\sigma'_2 - \sigma'_3)^2 + (\sigma'_3 - \sigma'_1)^2}$  and notations TC and TE in Fig. 13 show the failure envelopes for triaxial compression and extension, respectively.

In the negative  $\psi_{\text{peak}}$  case (Fig. 13(a)), the stress path at material point P3 (or C2) results in significant reduction in mean effective stress value during the initial shear band formulation (until 0.5 s) when there are higher excess pore water pressures. Once the excess pore pressure starts to dissipate after 0.5 s, the mean effective stress increases and finally reaches a magnitude larger than the initial values.



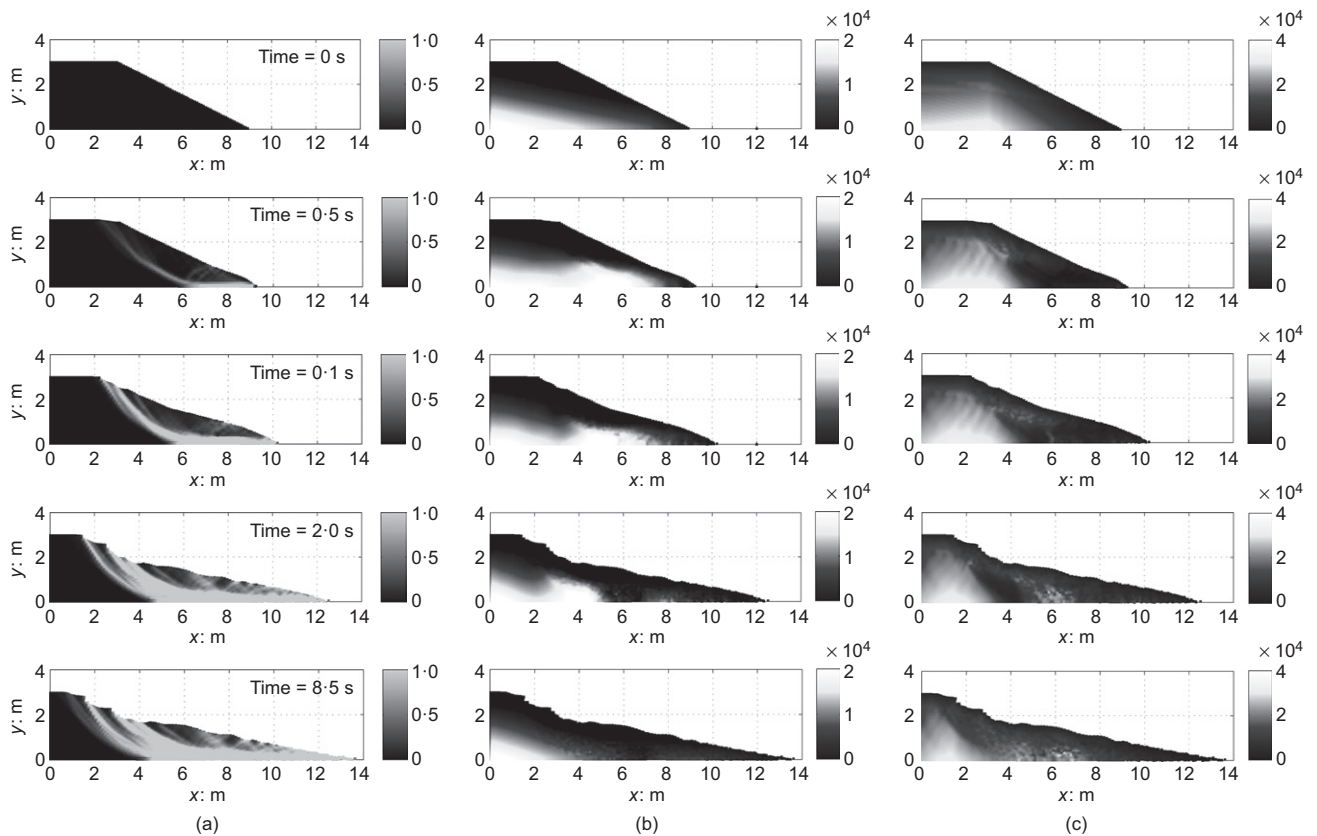


Fig. 8. Failure behaviour of levee with negative dilation angle  $\psi_{\text{peak}} = -1^\circ$ : (a) deviatoric shear strain variation; (b) pore pressure variation (Pa); (c) vertical effective stress variation (Pa)

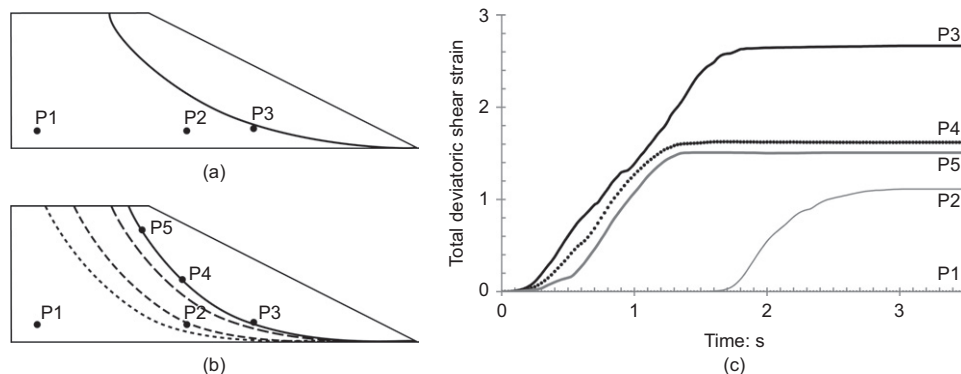


Fig. 9. Failure mechanisms of levees with different dilation angles: (a) shear band development for levee with zero dilation angle; (b) shear band development for levee with negative dilation angle  $\psi_{\text{peak}} = -1^\circ$ ; (c) deviatoric shear strain variation at locations for levee with  $\psi_{\text{peak}} = -1^\circ$

This is due to the fact that the final location of the material point is different from the initial location and it has a higher height of overburden. In the zero dilation case (Fig. 13(b)), both  $p'$  and  $q$  values gradually increase to the final values since the levee undergoes a smooth failure mechanism.

Results from the above-mentioned simulations have shown the capability of the two-layer MPM approach to model fully coupled problems that undergo rapid failures. This approach was able to capture the failure, the post-failure and the deposition stages, which are essential features to consider in landslide analyses. Use of a more advanced soil constitutive model could be helpful to obtain more accurate results.

#### SELBORNE SLOPE FAILURE SIMULATION BY SOIL–WATER TWO-PHASE USING ONE-LAYER MPM

Another case study on the MPM modelling of landslide failure is given in this section, where the failure and the

post-failure behaviour are integrated into a common analysis. The real slope remained nearly saturated from the beginning of the experiment until the end of the instability except for some points close to the toe. For this reason the simulation was conducted using the single-layer MPM (Jassim *et al.*, 2013) to represent a fully saturated soil. Each material point carries information on both the solid and the fluid phases and moves attached to the solid skeleton.

#### Selborne slope failure experiment

The Selborne slope failure experiment (Cooper, 1996; Cooper *et al.*, 1998), which was conducted with the purpose of investigating the nature of progressive failure in over-consolidated clays, was simulated. Some of the relevant field observations will be the benchmark data to compare model response and field data, as follows

- (a) the simultaneous development of failure conditions starting at the toe and the crest of the slope  
 (b) the recorded time history of pore pressures in the vicinity of the failure surface

- (c) the geometry of the failure surface, described as a compound sub-circular surface  
 (d) the measured displacements of some points of the slope surface after the failure.

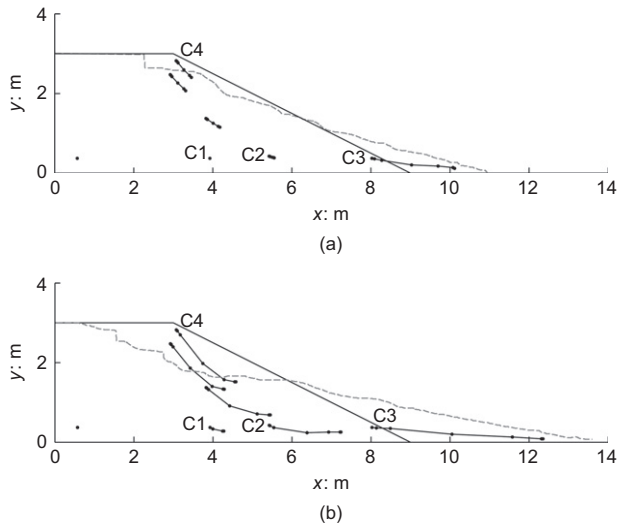


**Fig. 10.** Motion of material points at different locations for the levees with different dilation angles at peak: (a)  $\psi_{\text{peak}} = 0^\circ$ ; (b)  $\psi_{\text{peak}} = -1^\circ$

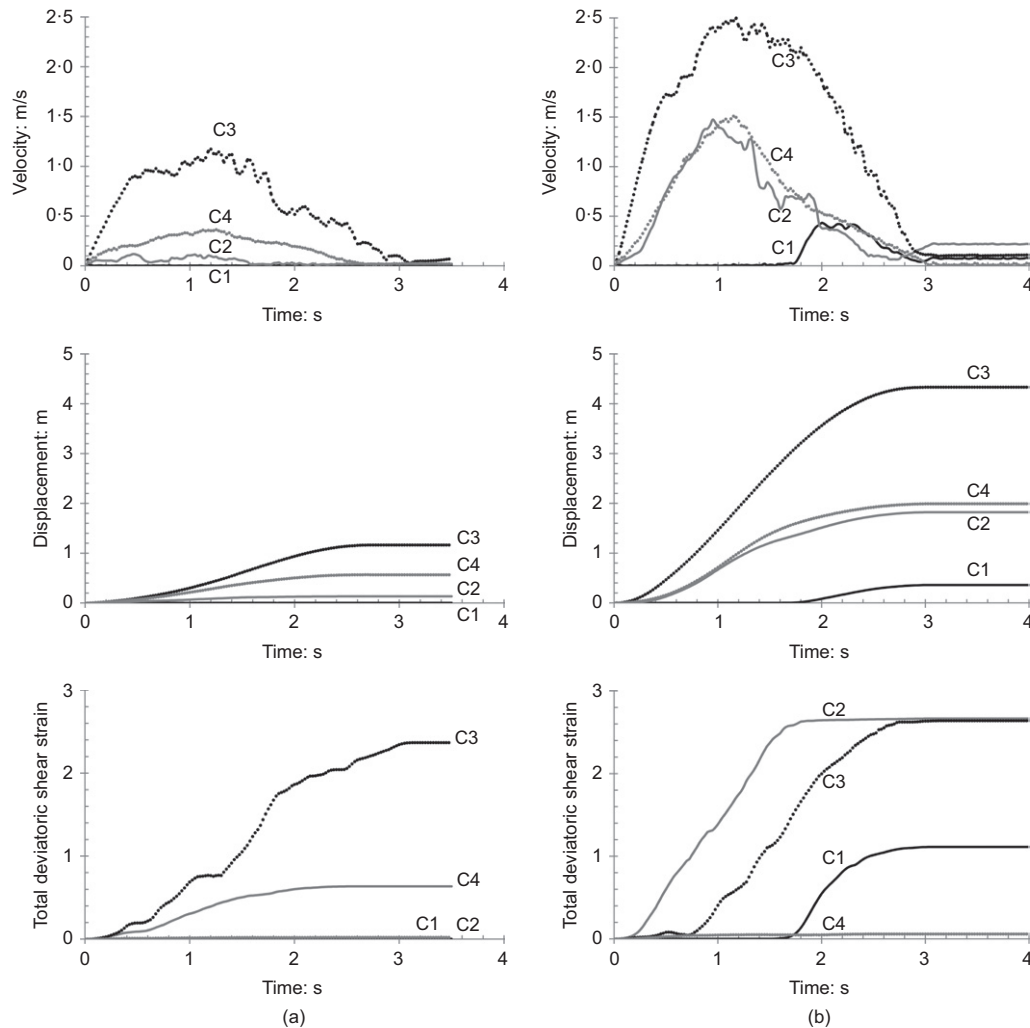


**Fig. 11.** Velocity, displacement and total deviatoric shear strain variations of material points C1, C2, C3 and C4 for the levees with different dilation angles at peak: (a)  $\psi_{\text{peak}} = 0^\circ$ ; (b)  $\psi_{\text{peak}} = -1^\circ$

The Selborne experiment was carried out in 1989 (Cooper, 1996) and it was designed to induce failure in a 9 m high, cut slope. A geological cross-section of the slope in a west-east direction is given in Fig. 14. The substratum is early Cretaceous unconsolidated sandstone (Lower Greensand). It is covered by a clay deposit (Gault Clay), which is over-consolidated, brittle, high-plasticity clay. Two layers can be distinguished within the clay deposit according to the degree of weathering. The upper weathered clay level is subdivided into Lower Gault Clay and Upper Gault Clay. A layer of soliflucted material covers the clay. Increasing the pore pressures within the slope initiated the slope failure. This was done by injecting water into the unweathered Gault Clay using vertical wells. The slope was instrumented using extensometers, piezometers and inclinometers in order to monitor the development of failure in the brittle clay. Precise surveying and inclinometers provided indications on the development of a progressive failure mechanism (Cooper, 1996; Grant, 1996).

#### The MPM model

As shown in Fig. 15, a background mesh that consists of thin, three-dimensional (3D), tetrahedral elements is used

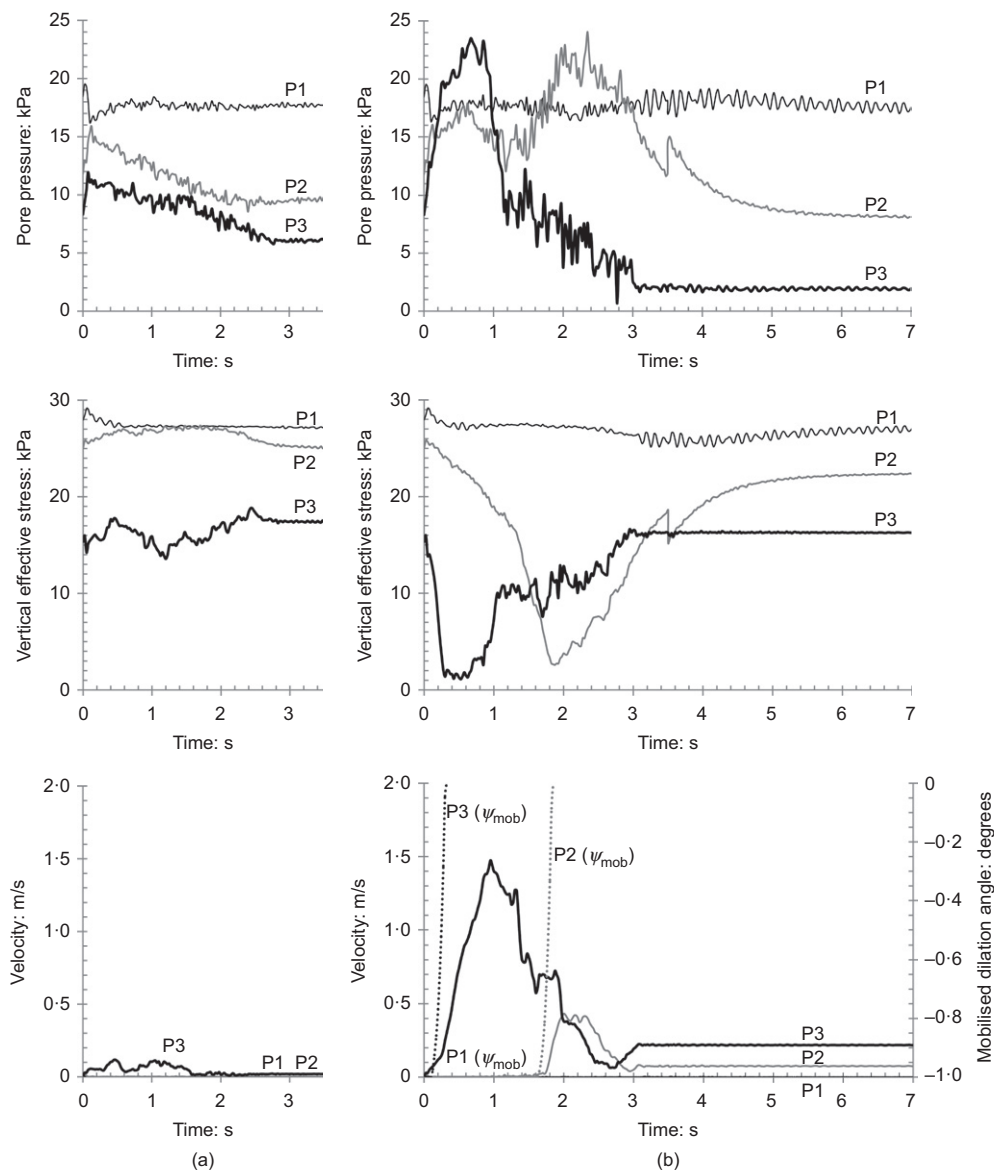


**Fig. 12.** Pore pressure, vertical effective stress and velocity behaviour at three different material point locations for the levees with different dilation angles at peak: (a)  $\psi_{\text{peak}} = 0^\circ$ ; (b)  $\psi_{\text{peak}} = -1^\circ$

and 6480 material points are placed in the original slope position. The mesh is refined in the domain where failure is expected. The horizontal displacements along the vertical side boundaries are fixed to be zero and the bottom boundary displacement is fixed in both directions. The soil is saturated throughout the calculation. The water pressure is kept to zero along the ground surface and the other boundaries are impervious.

The initial excavation and the subsequent period until the initiation of the failure experiment (5 months) were not simulated. Therefore, some differences between the actual initial stress state in the slope and the assumed gravity-related distribution is expected.

The initial pressure field is in equilibrium with a zero water pressure applied to the ground surface boundary. In order to simulate the artificial recharge, an excess of pore pressure was applied along the lower boundary (see Fig. 15). This excess pressure rises linearly during 10 s, up to 110 kPa, and after this time, it is maintained constant throughout the calculation. Because the numerical scheme is explicit, the calculation is conditionally stable and the time step increments are very small. For this reason, the permeability used in the simulation is several orders higher than the real one.

While the Selborne failure took place on the 196th day after the beginning of the water recharge, in the MPM calculation the instability occurs 39 s after starting the water loading. In order to compare the measured data with the numerical results, time ( $t_{\text{numerical}}$ ) has been normalised by the failure time ( $T$ )

$$t^* = \frac{t_{\text{numerical}}}{T} \quad (1)$$

#### Constitutive model

The model consists of two clay layers; weathered Gault Clay and unweathered Gault Clay. The laboratory testing programme by Cooper *et al.* (1998) provided several geotechnical properties that are summarised in Table 3. Both weathered and unweathered materials are characterised by a brittle behaviour, and both peak and residual effective shear strength parameters were also measured. A strain-softening constitutive model based on a non-associated Mohr–Coulomb law was used to simulate the brittleness of the overconsolidated Gault Clay. Softening behaviour is accounted for by reducing the strength parameters (effective

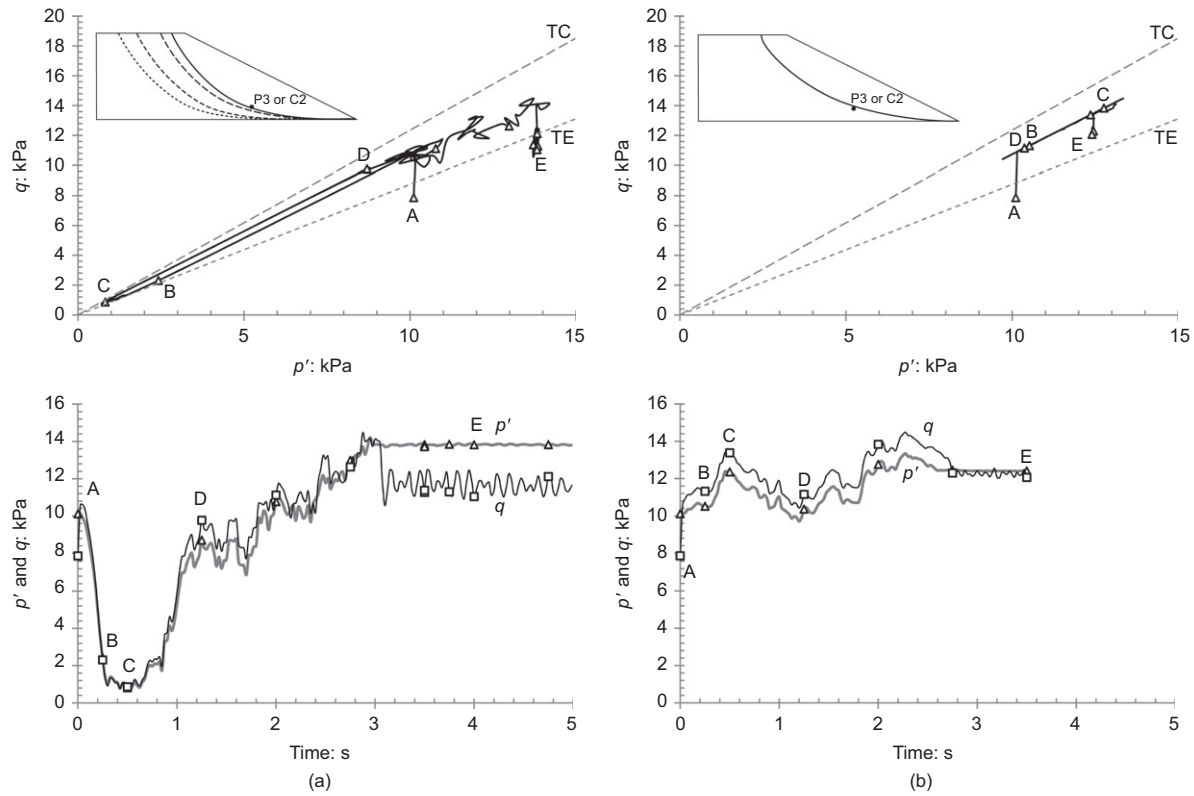


Fig. 13. Stress path  $p'$ - $q$  of point P3 (or C2) for levees with different dilation angles at peak: (a)  $\psi_{\text{peak}} = -1^\circ$ ; (b)  $\psi_{\text{peak}} = 0^\circ$

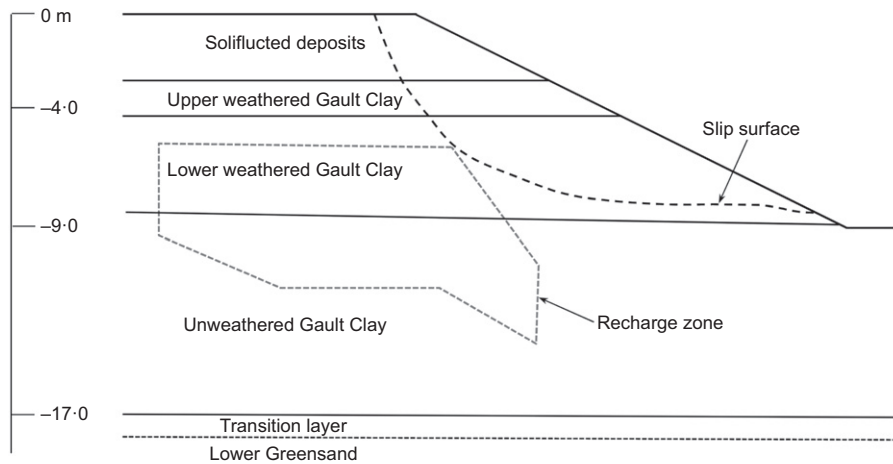


Fig. 14. General scheme of the centreline soil profile, recharge zone and estimated slip surface (based on Grant, 1996)

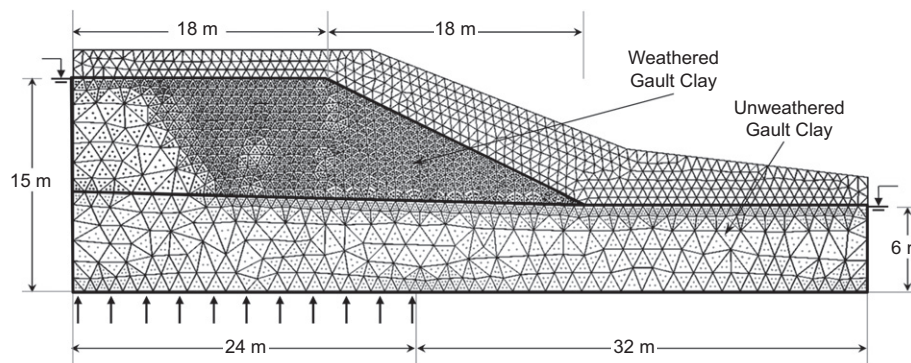


Fig. 15. Initial geometry and material points' distribution within the computational mesh (refined element size of 0.7 m). The location of the pressure boundary condition is also indicated



**Table 3. Geotechnical properties (based on Cooper *et al.*, 1998)**

	Soliflucted clay	Weathered Gault Clay		Unweathered Gault Clay
		Upper	Lower	
Liquid limit: %	70–75	70–75	60–65	60–65
Plastic limit: %	22	22	22	22
Water content: %	35	30–35	20–30	18
Deformation modulus: MPa	—	20–35	20–25	15–40
Effective peak cohesion: kPa	5	10	15	25
Effective residual cohesion: kPa	0	0	0	0
Effective peak friction angle: degrees	21	24	25	26
Effective residual friction angle: degrees	13	13	14	15

friction angle  $\phi'$  and effective cohesion  $c'$ ) with accumulated equivalent plastic strains  $\varepsilon_{eq}^p$  according to the following softening rules

$$c' = c'_r + (c'_{peak} - c'_r)e^{-\eta\varepsilon_{eq}^p} \quad (2)$$

$$\phi' = \phi'_r + (\phi'_{peak} - \phi'_r)e^{-\eta\varepsilon_{eq}^p} \quad (3)$$

The model requires the specification of peak ( $c'_{peak}$ ,  $\phi'_{peak}$ ) and residual ( $c'_r$ ,  $\phi'_r$ ) strength parameters. A 'shape factor' parameter  $\eta$  is also necessary in order to control the rate of strength decrease. The modifications proposed by Abbo & Sloan (1995) were introduced in the analysis to avoid difficulties associated with singular points of the yield surface. Parameters of the strain-softening Mohr–Coulomb constitutive model simulating the brittle behaviour of the clays are summarised in Table 4. The dilatancy angle was set to zero.

It is well known that the inclusion of strain-softening features in standard continuum numerical methods leads to mesh-dependent strain localisation problems (Oliver & Huespe, 2004). A smeared crack approach (Rots *et al.*, 1985) has been used as a regularisation technique. It postulates that the total work dissipated by a shear band of thickness  $h$  ( $W_h$ ) is equivalent to the fracture energy dissipated in a theoretical discrete crack ( $G$ ); hence  $G = W_h$ .

In MPM the thickness of a shear band  $h$  can be approximated by the mesh element size. Then, in order to avoid the mesh size dependence and according to the smeared crack approach concept, the work dissipated by a shear band formed by elements of thickness  $h_1$  ( $Wh_1$ ) should be equal to the work dissipated by another shear band of thickness  $h_2$  ( $Wh_2$ ). Then  $G = Wh_1 = Wh_2$ . To be consistent, the constitutive modulus of the material should depend on the mesh element size.

One way to include this dependence is to carry out a set of numerical shear tests with different element mesh sizes. The bottom of the sample is fixed and a horizontal prescribed velocity is applied at the top, ensuring that the final relative displacement between both sides of the band ( $U_x$ ) is enough to degrade the material down to its residual state. Then, a calibration of the shape factor  $\eta$  can be performed in order to ensure that the dissipated work is the same for different element sizes discretising the band.

The work dissipated in the shear band (per unit length) can be written as

$$W_h = \int_0^{U_x} \tau \, du_x \quad (4)$$

The dissipated work is the area defined under the curve  $\tau$ – $U_x$  in Fig. 16(b); hence two different shear bands dissipate the same energy when areas  $A_1$  and  $A_2$  are equal (see Figs 16(a) and 16(b)).

**Table 4. Material parameters of the modelling**

	Weathered Gault Clay	Unweathered Gault Clay
Porosity	0.38	0.38
Permeability: m/s	0.001	0.001
Solid density: kg/m <sup>3</sup>	2700	2700
Young's modulus: kPa	20 000	20 000
Poisson ratio	0.33	0.33
Effective peak cohesion: kPa	13	25
Effective residual cohesion: kPa	4.7	0.5
Effective peak friction angle: degrees	24.5	26
Effective residual friction angle: degrees	13.5	15
Shape factor	400	400

Figure 16(c) shows the calibrated relationship  $\tau$ – $U_x$  for three different thicknesses of the shear band ( $h=1.0$  m,  $h=0.7$  m and  $h=0.5$  m). Note that the larger the element size, the higher the shape factor.

Under unsaturated conditions, the strength increases due to the suction effect, especially the cohesive component. When soil is close to saturated conditions, the additional cohesion due to suction  $c_{suction}$  can be estimated as

$$c_{suction} = s \tan \phi' \quad (5)$$

where  $s$  is the suction and  $\phi'$  is the effective friction angle. The residual cohesion of the weathered clay is given a positive, albeit small, value (4.7 kPa). This value was determined based on the negative pore water pressures measured in the vicinity of the final failure surface (between 0 and –42 kPa) (Cooper, 1996).

### Results

Figure 17 shows the evolution of the incremental pore water pressure at three different points within the slope up to the failure ( $t^*=1$ ). Numerical results are compared with field data (Bromhead *et al.*, 1998). The agreement is quite reasonable, especially in piezometers B and C. Note that increments in pore pressure above the initial values are plotted. The initial pore pressures in the model resulted from an initial saturation of the slope. However, the actual piezometer records show negative pore pressures in several locations. Field data as well as calculations show a decrease in pore pressure in the vicinity of the failure time. Cooper *et al.* (1998) attributed this decrease to dilatancy. However, model calculations were run for the zero dilatancy condition. In this simulation, the decrease in calculated pore pressure is attributed to a volumetric extension state in locations shown in Fig. 17. If some dilatancy is included in the model (like the

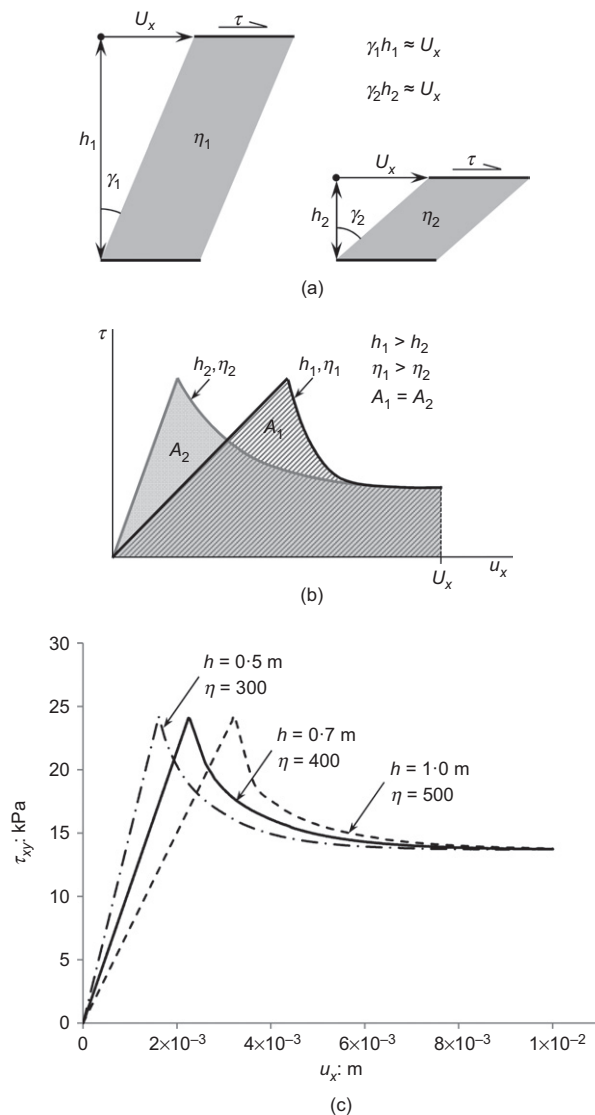


Fig. 16. Calibration of the shape factor  $\eta$  of two shear bands with different thickness ( $h_1$  and  $h_2$ ). (a) Scheme of the two bands after being deformed with the same relative displacement  $U_x$ . (b) Relationship  $U_x$  for both shear bands with different shape factors  $\eta$ . (c) Calibrated relationship  $\tau-U_x$  for three different mesh sizes ( $h = 1.0$  m,  $h = 0.7$  m and  $h = 0.5$  m)

levee case discussed in the previous section), a more intense decrease in pore pressure is predicted.

In addition to mesh-dependent strain-localisation problems, separation and splitting in an MPM discretisation also depends on the mesh size because the material points remain numerically 'in contact' whenever they have a node in common. This fact may lead to non-physical increase of material stiffness when two points tend to separate (Huang *et al.*, 2011).

Three different refined meshes were analysed to evaluate the effect of the mesh size on the results ( $h$ ): 1 m, 0.7 m and 0.5 m. In order to minimise the mesh dependency, the shape factor  $\eta$  was calibrated as described previously. Fig. 18 illustrates the final geometry and the displacement field once the slope stops for the three MPM calculations, showing that the slope response becomes essentially mesh independent. The sliding surface measured in situ is also shown. Fig. 19 shows the total displacement of the crest point becomes independent of the mesh size. However, if the same shape factor is adopted for all meshes, the smaller the element size, the higher are the calculated displacements after the failure.

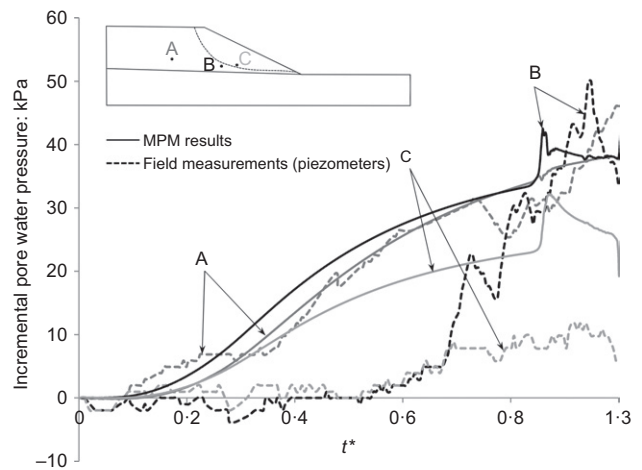


Fig. 17. Evolution of the incremental pore water pressure at three different points within the slope. Solid lines represent MPM simulation and dashed lines represent field data (Bromhead *et al.*, 1998). Time is dimensionless ( $t^*$ )

The initial failure mechanisms obtained with the three meshes are compared with the measured slip surface in more detail in Fig. 20. It is clear that the geological discontinuity between weathered and unweathered clay plays an important role in the failure geometry. The lower part of the slip surface is almost horizontal following the contact, although it is included completely in the weathered layer. Numerical results indicate that the failure mechanism is located slightly deeper into the slope than the measurements. This could be an effect of the orientation of element faces in the MPM mesh discretisation. The initial failure mechanism also depends on the stress field. Therefore, some differences can be expected between numerical results and measurements because the initial excavation is not simulated in this analysis.

Material point method-predicted surface horizontal displacements at the end of the failure are compared with measurements in Fig. 21. Because the purely 2D failure regime was not achieved in the Selborne failure, data have been grouped into two zones (north and south). The order of magnitude as well as the distribution of the calculated horizontal displacements fit very well with field data on the southern side. The north side appears to provide some restraint to the motion.

In view of the calculations carried out with three different meshes (Figs 18–21) it was realised that a 0.7 m mesh size was appropriate to analyse the Selborne experiment. In addition, the central processing unit (CPU) time consumed for this mesh is acceptable (see CPU times in Fig. 19).

The whole instability process is illustrated in Fig. 22. The evolution of equivalent plastic strain, excess pore pressure and vertical effective stress is shown at five normalised times ( $t^*$ ). Note that some scales vary in order to capture the results properly.

#### Progressive failure

The interpretation of several inclinometer profiles (Cooper, 1996) indicated that the failure surface developed progressively in the manner proposed by Bishop (1971). The shearing localisation progressed simultaneously from the higher and lower parts of the final slip surface towards the central part. Following the idea of Skempton (1964), a mobilised friction  $\hat{\phi}'$  is defined

$$\sin \hat{\phi}' = \frac{q}{p^*} \quad (9)$$

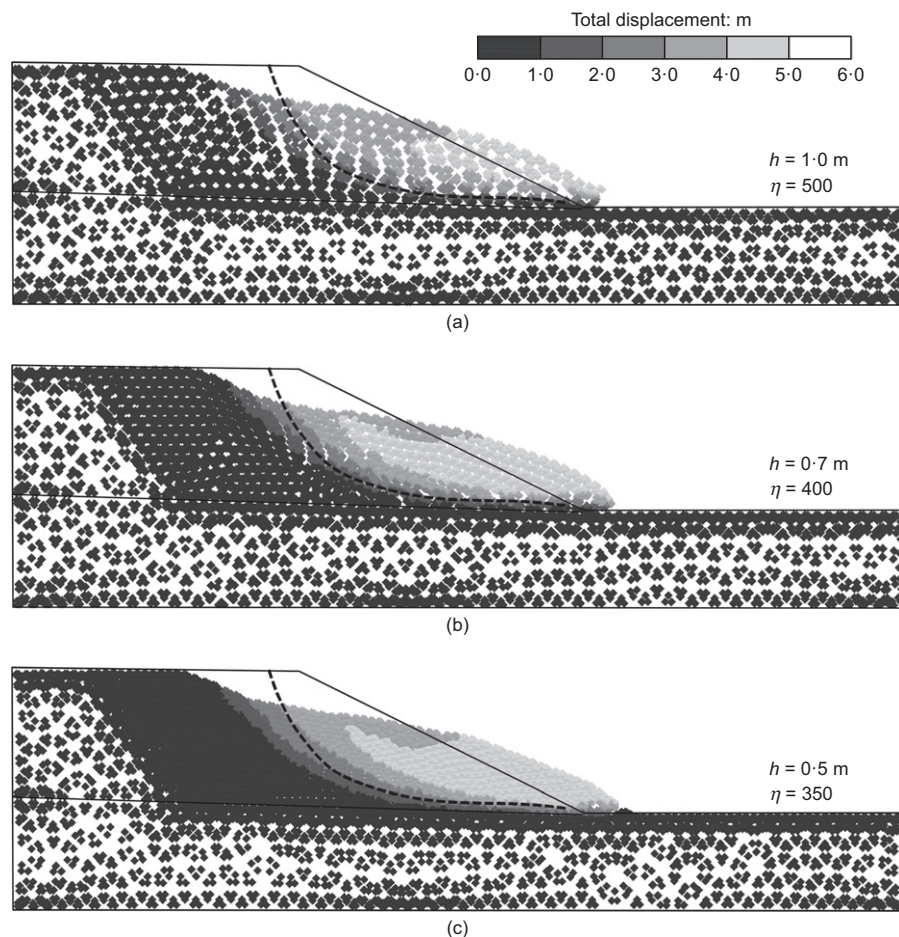


Fig. 18. Final distribution of the material points and displacement fields for the three MPM calculations: (a)  $h = 1.0$  m; (b)  $h = 0.7$  m; (c)  $h = 0.5$  m of refined element size. The slip surface measured in the field is indicated by the dashed line

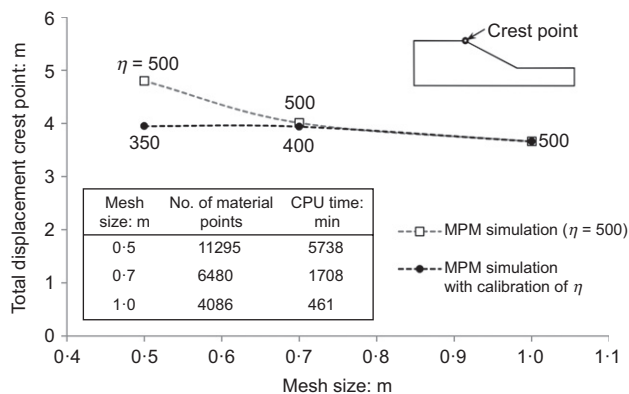


Fig. 19. Total displacement of crest point depending on mesh size in which the effect of calibration on the shape factor  $\eta$  is shown. Number of material points and CPU time are included for the three meshes

where  $p^* = p' + c'/\tan \phi'$ ,  $p' = (\sigma'_1 + \sigma'_3)/2$  and  $q = (\sigma'_1 - \sigma'_3)/2$ . Note that the definitions of  $p$  and  $q$  here are different from the previous case.

This measure of the mobilised strength allows comparison of the evolution of stresses of points belonging to the failure surface. The mobilised friction angle along the initial failure mechanism has been determined for different times. Fig. 23 provides a clear view of the progressive failure phenomenon. Initially all material points are in elastic regime (Fig. 23(b)). As water pressure increases,  $\phi'$  approaches the peak value. P2 is the first point to reach the peak yield surface at  $t^* = 0.81$

(Fig. 23(c)). The failure propagates and at  $t^* = 0.85$  the upper part of the shear band (P1, P2) is at residual conditions. At this time, the toe of the slope (P7) also reaches the peak conditions (Fig. 23(c)). Afterwards, the progressive failure stops, whereas the shear stressing increases within the elastic range in the central part of the slide surface. Progressive failure is resumed at  $t^* = 0.953$  and it progresses from the toe to the centre part of the slope (plastic points P6, P5 and P4) (Fig. 23(d)). Finally, the failure mechanism is completed and the entire failure surface approaches residual conditions. Immediately after, the sliding motion starts. Even if the numerical simulation performed does not consider the effects of the initial excavation, it is clear that a comparison of Fig. 23 with the progressive mechanisms described in Cooper (1996) reveals that both failures develop in a similar way: the higher and the lower part of the slope plasticise first and finally the central part reaches residual conditions.

A significant improvement over static formulations is that the dynamic behaviour of the slide instability can be analysed in conjunction with the pre-rupture phenomenon. The calculated motion paths, total displacement, velocity and acceleration of points C1, C2, C3 and C4 (Fig. 24(a)) are shown in Figs 24(b)–24(d). When analysing these plots it can be observed that the embankment remains stable until  $t^* = 1$ . When the failure mechanism develops those material points located above the shear band (C1, C2 and C3) accelerate quickly and a peak velocity is attained at  $t^* = 1.1$ . Afterwards, the acceleration becomes negative and the velocity decreases towards a new state of equilibrium. At  $t^* = 1.2$  the slope tends to stabilise. Note that the dynamic variables depend on the position of the point within the slope: C4 remains motionless

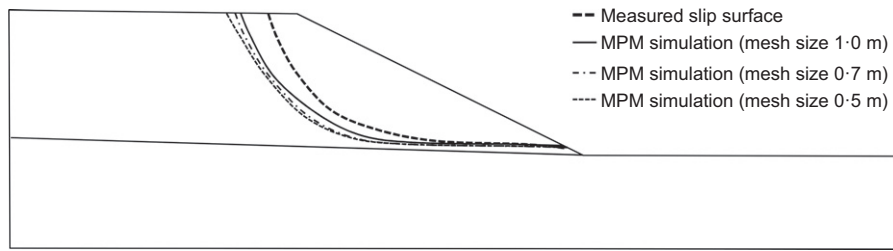


Fig. 20. Comparison between the initial failure mechanisms obtained with the MPM simulations and the measured slip surface

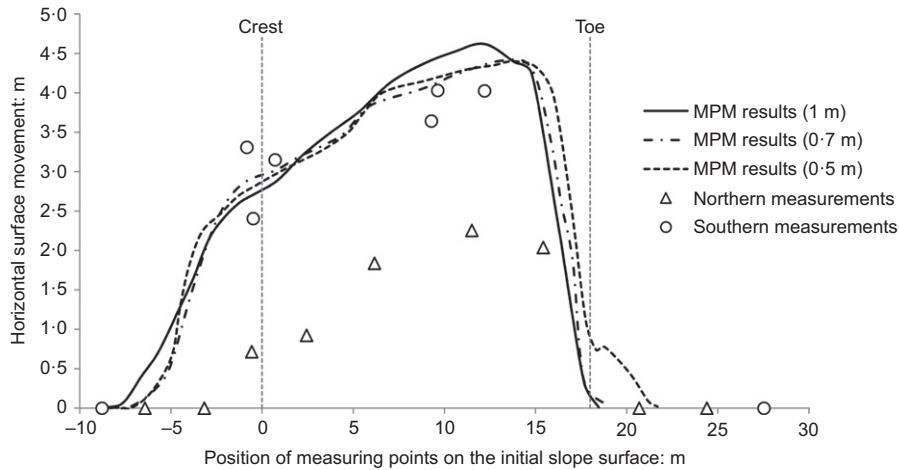


Fig. 21. Comparison between measured surface movements with the horizontal displacements obtained with the MPM calculations

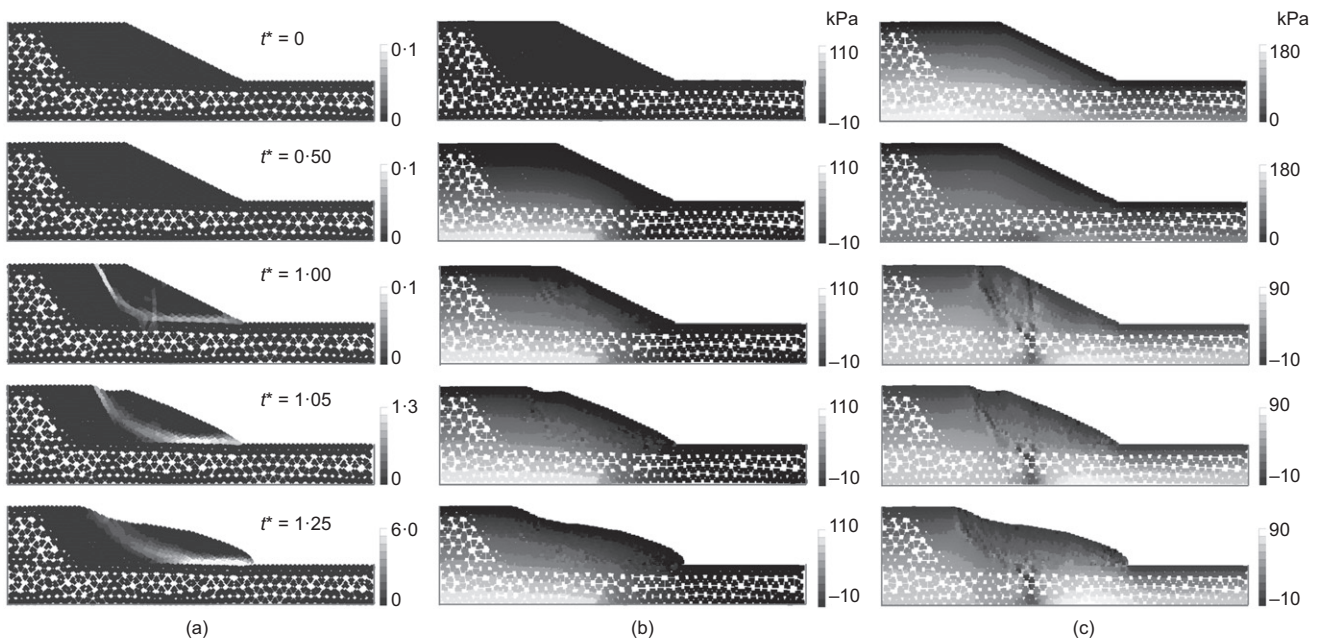


Fig. 22. Results of the Selborne experiment modelling at different normalised times (refined mesh size of 0.7 m): (a) equivalent plastic strain; (b) excess pore pressure (kPa); (c) vertical effective stress (kPa)

during all the calculation and C3 initially at the slope toe moves a small distance. In fact, soil located above the toe level rolls over the toe. The model indicates that the maximum sliding velocity was around 0.83 m/s in the middle and upper parts of the slope.

#### Behaviour at material points

The stress path  $p'$ - $q$  of the material points P2 and C4 are represented in Figs 25(a) and 25(c), respectively, in which

peak and residual Mohr–Coulomb yield surfaces have also been included. P2 is located in the weathered clay layer, whereas C4 is in the unweathered material. Starting at an initial gravity-induced elastic stress state, the effective volumetric stress  $p'$  reduces in P2 due to the rise of pore pressure along part of the lower boundary. Afterwards, the shear stress  $t$  slightly increases until the peak yield surface is reached. At this point, the softening process reduces the strength down to residual conditions, while pore pressures continue to increase (Figs 25(a) and 25(b)). During the movement, the stresses



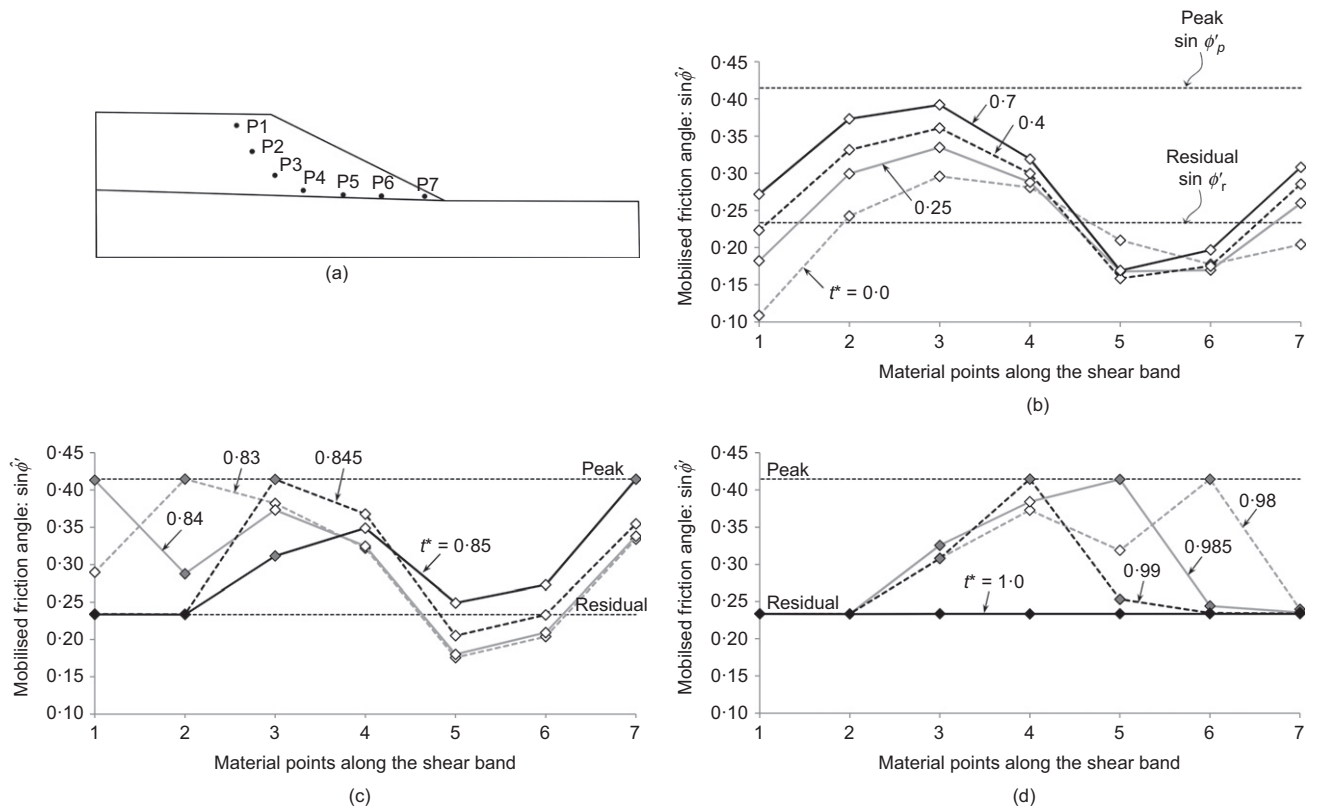


Fig. 23. Distribution of the mobilised friction angle along seven material points located in the initial shear band (a) at different moments: (b) elastic loading; (c) progressive failure initialisation; (d) final part of the progressive failure. Time is dimensionless ( $t^*$ )

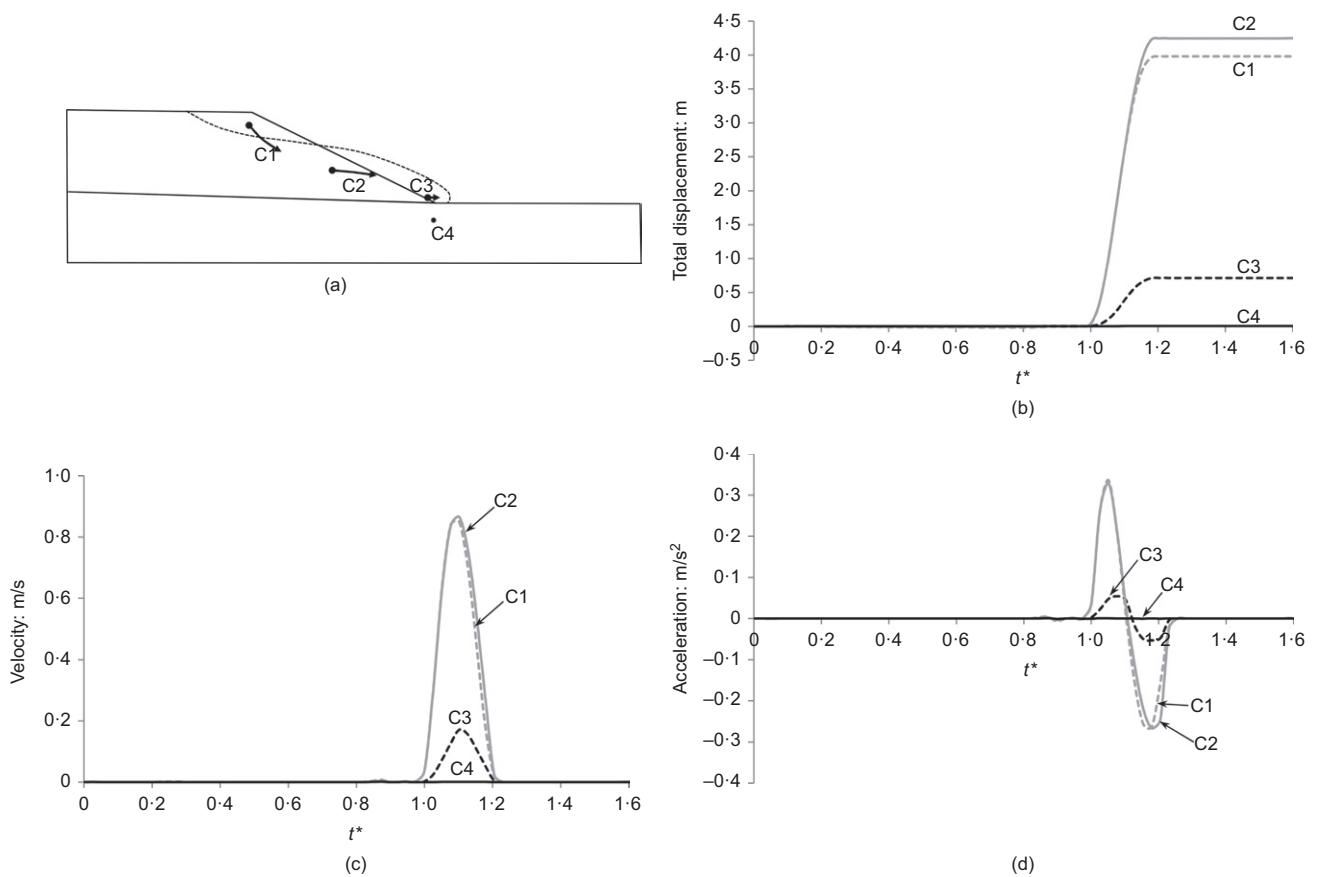


Fig. 24. (a) Motion paths of material points C1, C2, C3 and C4. Evolution of (b) total displacements; (c) velocities; (d) accelerations of C1, C2, C3 and C4

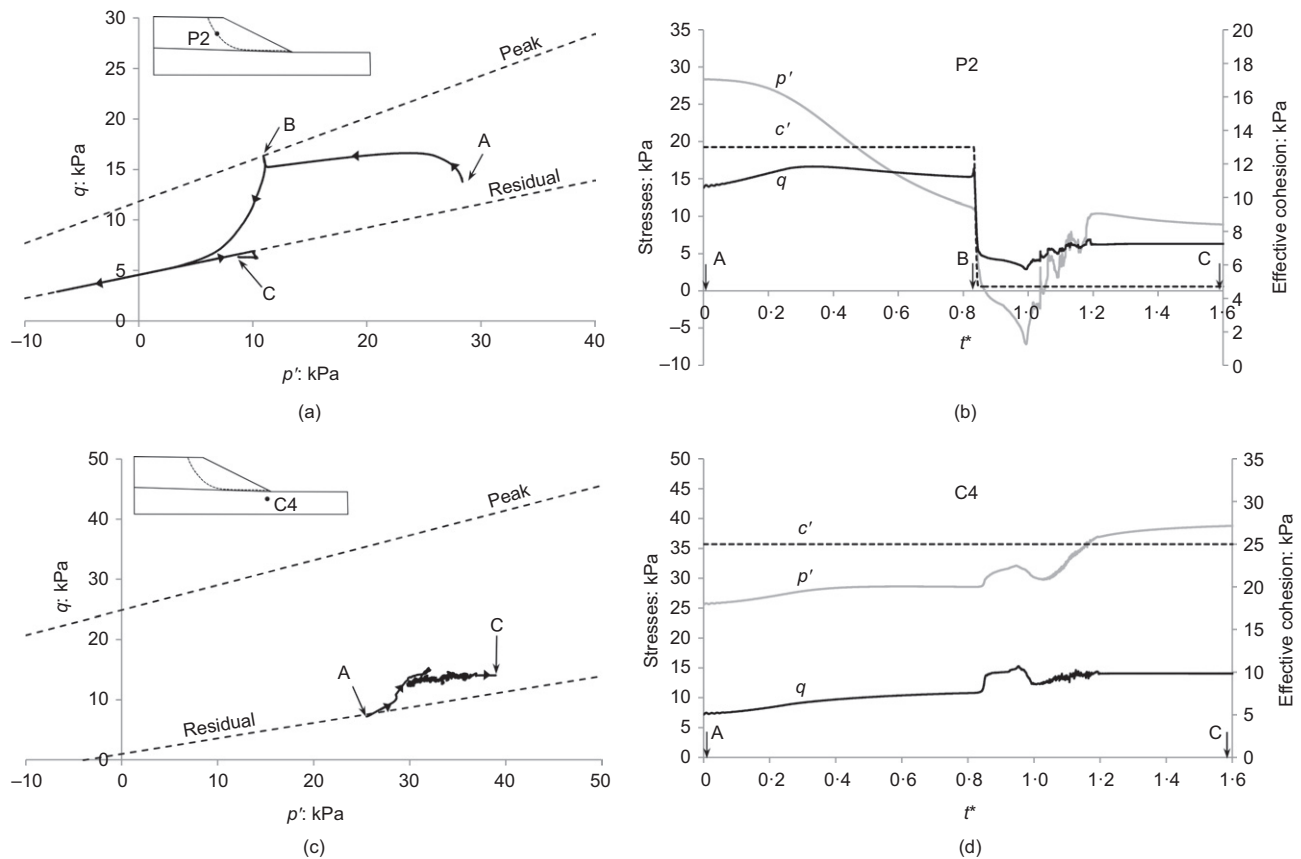


Fig. 25. Stress path  $p'-q$  of points P2, P5 and C4. Time is dimensionless ( $t^*$ )

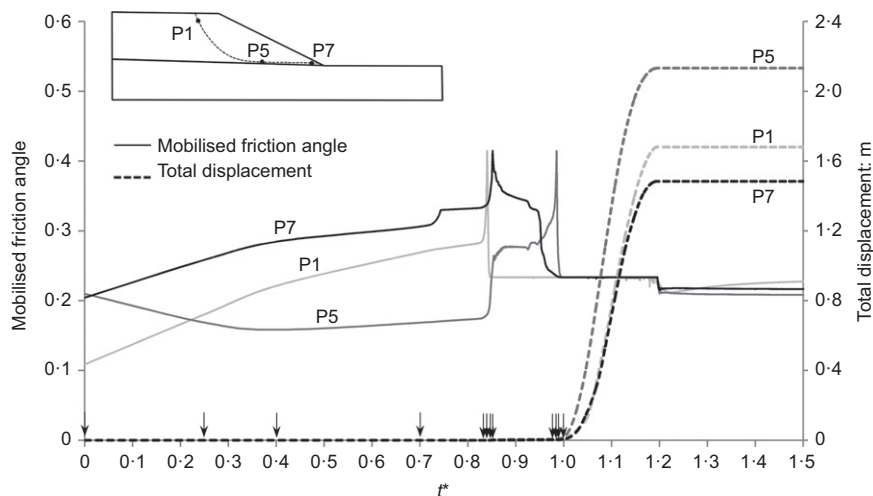


Fig. 26. Overall instability process. Evolution of mobilised friction angle (solid line) and total displacement (dashed line) of three material points initially located within the shear band (P1, P5 and P7). Reference times plotted in Fig. 23 are indicated with vertical arrows

vary but remain in residual conditions. Finally, when the slope is stabilised, the stresses relax slightly and P2 comes back to the elastic region. Point C4 behaves in a different manner. Because it is located under the toe of the slide, far from the water recharge,  $p'$  does not decrease and it remains in elastic conditions throughout all the calculation. On the contrary,  $p'$  increases due to stacked material lying on top of it at the end of the instability.

In order to provide an overall view of the slope instability, Fig. 26 shows in a unified way the progressive failure process, the stress evolution and the kinematic behaviour of the slide. The evolution of mobilised friction angle and total

displacement of three selected material points initially located at the shear band (P1, P5 and P7) are presented. In addition, vertical arrows indicate reference times of Fig. 23. Some time is needed until the water pressure is high enough to bring some points to a failed state. Between  $t^* = 0.83$  and  $t^* = 0.85$  progressive failure starts at the higher part (P1) and the toe (P7) of the slope. The progressive shear localisation reactivates along the base and the central part of the failure mechanism (P5). Residual strength conditions along the entire failure surface are necessary to initialise the motion of the slope at  $t^* = 1.0$ . Immediately after the reactivation of the shear localisation, total displacements increase rapidly with

the motion and all points of the sliding surface remain at residual conditions. Finally, a new stable geometry is achieved at  $t^* = 1.2$  and the slope ceases to flow. Some points experience a small unloading and become elastic.

## CONCLUSIONS

Traditional geotechnical analyses for landslides involve failure prediction (i.e. on-set of failure) and the design of structures that can safely withstand the applied loads. However, they provide limited information on the post-failure behaviour. Modern numerical techniques are capable of simulating large mass movements and there is an opportunity to utilise such techniques to assess the risk of catastrophic damage due to a landslide. In this paper, various large-deformation analysis methods are introduced and their applicability to landslide problems is discussed.

Catastrophic landslides often involve seepage forces and hence consideration of the coupled behaviour of soil and pore fluid is essential. In this paper, different numerical techniques to model large deformation are introduced to provide a reference point for the readers to understand the research trend in this area. In particular, MPM was selected as the authors' choice, primarily because: (a) the implementation is intuitive for users of FEM; (b) it can incorporate advanced history-dependent soil constitutive models; and (c) its application of boundary conditions is more straightforward than other mesh-free methods owing to the presence of the background grid.

Two approaches to model soil–pore fluid coupling are introduced and an example simulation is presented for each approach. One example is for a model levee failure and the other is on a natural cut slope failure (the Selborne experiment). In the levee failure case, MPM simulation was able to capture the complex failure mechanism that includes the development of successive shear bands while predicting excess pore pressure generation during the failure propagation, and finally the consolidation stage. The simulations demonstrated the importance of the dilation characteristics of soil as well as changes in geometry for post-failure behaviour. In the Selborne case, MPM was able to simulate the progressive failure of the brittle, overconsolidated clay. It showed the evolution of shear stresses along the failure surface. The changes in pore pressure at some specific locations and the actual shape of the failure surface were well captured. The importance of modelling the shear band accurately within the MPM framework is highlighted.

The single-layer two-phase MPM formulation is computationally more efficient than the two-layer formulation. If the fluid flow within a soil and its geotechnical consequences are the major concern, it is an effective method. The two-layer formulation ensures that the masses of both soil and water are conserved. It can be used to model various interactions of soil and water explicitly. Examples include soil fluidisation and erosion in a submerged soil system due to dynamic water movements at the interface, internal soil erosion and sand production process due to seepage, and so on. However, it requires more computational time than the single-layer two-phase MPM formulation.

Although the example cases described in this paper demonstrate the potential opportunities for large-deformation analysis to predict both pre- and post-failure behaviour of landslides, further work is required to develop the confidence of geotechnical engineers in using such tools in their engineering practice. For example, further improvement is needed to ensure that the coupled analysis can be performed with limited numerical errors and in a more computationally efficient manner. The feasibility of available soil constitutive models for large-deformation analysis needs to be investigated. In particular, it is necessary to model the unsaturated

soil behaviour accurately, because many of the regions that undergo landslides are unsaturated in the beginning. More case studies are needed to understand their capabilities and limitations. Finally, further work is needed to show the capabilities and limitations of the two formulations presented in this paper.

## ACKNOWLEDGEMENTS

The code used in the modelling of the Selborne failure experiment is a version of the MPM code developed at Deltares (Delft) as well as by the other remaining members of the MPM Research Community: Universitat Politècnica de Catalunya, University of Cambridge and Technische Universität Hamburg-Harburg. Results from the Selborne Project (Cooper *et al.*, 1998) are used with the permission of the investigators. The UK Engineering and Physical Science Research Council funded their project.

## NOTATION

$a_{ws}$	fluid acceleration with respect to the soil skeleton
$c'$	effective cohesion
$c'_{u,mob}$	mobilised capillary cohesion
$E$	Young's modulus (Pa)
$G$	fracture energy dissipated in a theoretical discrete crack
$h$	shear band thickness
$k_0$	initial permeability (m/s)
$\mathbf{m}$	Kronecker delta vector
$m_p$	mass of a material point 'p'
$p$	pressure
$p'$	mean effective stress
$p^*$	$p^* = p' + c'/\tan \phi'$
$q$	deviatoric stress
$S_w$	saturation ratio
$s$	suction
$T$	field time for failure
$t_k$	current time step
$t_{numerical}$	equivalent numerical time
$t_0$	reference time
$t^*$	normalised time
$U_x$	final relative displacement between both sides of a shear band
$u$	displacement
$u_x$	relative displacement between both sides of a shear band
$V_p$	volume of a material point 'p'
$v_p$	velocity of a material point 'p'
$v_s$	volume of solids
$v_w$	volume of water
$W_h$	work dissipated in the shear band (per unit length)
$X_i$	computational node 'i' of the grid in material point method
$x_p$	position of a material point 'p'
$\alpha$	(friction / dilation / cohesion)
$\gamma_{dev,pl}^{crit}$	plastic deviatoric strain at critical state
$\gamma_{dev,pl}^{peak}$	total plastic deviatoric strain
$\gamma_{dev,pl}^{peak}$	plastic deviatoric strain at peak
$\epsilon_{eq}^p$	equivalent plastic strain
$\eta$	shape factor
$\eta_0$	initial porosity
$\nu$	Poisson ratio
$\rho_s$	solid grain density (kg/m <sup>3</sup> )
$\sigma'$	effective stress
$\phi'$	effective friction angle (degrees)
$\phi'_m$	mobilised friction angle
$\psi$	dilation angle
$\Omega$	domain
Subscripts	
crit	critical state
mob	mobilised
p	at material point
peak	peak
r	residual

## REFERENCES

- Abbo, A. & Sloan, S. (1995). A smooth hyperbolic approximation to the Mohr–Coulomb yield criterion. *Comput. Structs* **54**, No. 3, 427–441.
- Abe, K., Soga, K. & Bandara, S. (2013). Material point method for coupled hydromechanical problems. *J. Geotech. Geoenviron. Engng* **140**, No. 3, 04013033.
- Andersen, S. & Andersen, L. (2010). Modelling of landslides with the material-point method. *Comput. Geosci.* **14**, No. 1, 137–147.
- Augarde, C. & Heaney, C. (2009). The use of meshless methods in geotechnics. In *Proceedings of the 1st international symposium on computational geomechanics (ComGeo I)*, Juan-les-Pins, Cote d'Azur, France, pp. 311–320. Rhodes, Greece: IC2E. See [https://community.dur.ac.uk/charles.augarde/pubs/Augarde\\_Heaney\\_COMGEO1.pdf](https://community.dur.ac.uk/charles.augarde/pubs/Augarde_Heaney_COMGEO1.pdf) (accessed 05/11/2015).
- Bandara, S. (2013). *Material point method to simulate large deformation problems in fluid-saturated granular medium*. PhD thesis, University of Cambridge, Cambridge, UK.
- Bandara, S. & Soga, K. (2015). Coupling of soil deformation and pore fluid flow using material point method. *Comput. Geotech.* **63**, No. 1, 199–214.
- Basu, D., Das, K., Janetzke, R. & Green, S. (2011). Numerical simulations of non-Newtonian geophysical flows using smoothed particle hydrodynamics (SPH) method: a rheological analysis. In *Proceedings of ASME 2011 international mechanical engineering congress and exposition, IMECE 2011. Volume 6: fluids and thermal systems; advances for process industries, parts A and B*, pp. 155–164. New York, NY, USA: American Society of Mechanical Engineers (ASME).
- Belytschko, T., Lu, Y. Y. & Gu, L. (1994). Element-free Galerkin method. *Int. J. Numer. Methods Engng* **37**, No. 2, 229–256.
- Beuth, L., Benz, T., Vermeer, P. A. & Wiekowski, Z. (2008). Large deformation analysis using a quasi-static material point method. *J. Theor. Appl. Mech.* **38**, No. 1–2, 45–60.
- Beuth, L., Wiekowski, Z. & Vermeer, P. A. (2010). Solution of quasi-static large-strain problems by the material point method. *Int. J. Numer. Analyt. Methods Geomech.* **35**, No. 13, 1451–1465.
- Bishop, A. W. (1971). The influence of progressive failure on the choice of the method of stability analysis. *Géotechnique* **21**, No. 2, 168–172, <http://dx.doi.org/10.1680/geot.1971.21.2.168>.
- Blanc, T. & Pastor, M. (2012). A stabilized fractional step, Runge–Kutta Taylor SPH algorithm for coupled problems in geomechanics. *Comput. Methods Appl. Mech. Engng* **221–222**, 41–53.
- Bonet, J. & Kulasegaram, S. (2000). Correction and stabilization of smooth particle hydrodynamics methods with applications in metal forming simulations. *Int. J. Numer. Methods Engng* **47**, No. 6, 1189–1214.
- Bromhead, E. N., Cooper, M. R. & Petley, D. J. (1998). The Selborne cutting slope stability experiment. *Selborne data collection CD* (CD-ROM).
- Brown, K. H., Burns, S. P. & Christon, M. A. (2002). *Coupled Eulerian-Lagrangian methods for earth penetrating weapon applications*, Report SAND2002-1014. Albuquerque, NM, USA: Sandia National Laboratories.
- Bui, H. H., Fukagawa, R., Sako, K. & Ohno, S. (2008). Lagrangian meshfree particles method (SPH) for large deformation and failure flows of geomaterial using elastic-plastic soil constitutive model. *Int. J. Numer. Analyt. Methods Geomech.* **32**, No. 12, 1537–1570.
- Capecelatro, J. & Desjardins, O. (2013). An Euler–Lagrange strategy for simulating particle-laden flows. *J. Comput. Physics* **238**, 1–31.
- Cascini, L. & Cuomo, S. (2010). Modeling of rainfall-induced shallow landslides of the flow-type. *J. Geotech. Geoenviron. Engng* **136**, No. 1, 85–98.
- Cascini, L., Cuomo, S. & Guida, D. (2008). Typical source areas of May 1998 flow-like mass movements in the Campania region, Southern Italy. *Engng Geol.* **96**, No. 3–4, 107–125.
- Cascini, L., Cuomo, S., Pastor, M. & Sacco, C. (2013). Modelling the post-failure stage of rainfall-induced landslides of the flow type. *Can. Geotech. J.* **50**, No. 9, 924–934.
- Cascini, L., Cuomo, S., Pastor, M., Sorbino, G. & Piciullo, L. (2014). SPH run-out modelling of channelised landslides of the flow type. *Geomorphology* **214**, 502–513.
- Chemenda, A., Bois, T., Bouissou, S. & Tric, E. (2009). Numerical modelling of the gravity-induced destabilization of a slope: the example of the La Clapiere landslide, southern France. *Geomorphology* **109**, No. 3–4, 86–93.
- Cooper, M. (1996). The progressive development of a failure slip surface in over-consolidated clay at Selborne, UK. In *Proceedings of the 7th international symposium on landslides*, Trondheim, Norway (ed. K. Senneset), pp. 683–688. Rotterdam, the Netherlands: Balkema.
- Cooper, M. R., Bromhead, E. N., Petley, D. J. & Grants, D. I. (1998). The Selborne cutting stability experiment. *Géotechnique* **48**, No. 1, 83–101, <http://dx.doi.org/10.1680/geot.1998.48.1.83>.
- Cremonesi, M. & Perego, U. (2013). Numerical simulation of landslide–reservoir interaction using a PFEM approach. In *Particle-based methods III: fundamentals and applications – Proceedings of the 3rd international conference on particle-based methods – fundamentals and applications, Particles 2013, Stuttgart, Germany* (eds M. Bischoff, E. Ramm, E. Oñate, R. Owen and P. Wriggers), pp. 408–417. Barcelona, Spain: Barcelona International Center for Numerical Methods in Engineering.
- Cuomo, S., Prime, N., Iannone, A., Dufour, F., Cascini, L. & Darve, F. (2013). Large deformation FEM-LIP drained analysis of a vertical cut. *Acta Geotechnica* **8**, No. 2, 125–136.
- Daouadji, A., AlGali, H., Darve, F. & Zeghloul, A. (2010). Instability in granular materials: experimental evidence of diffuse mode of failure for loose sands. *J. Engng Mech.* **136**, No. 5, 575–588.
- Darve, F. & Laouafa, F. (2000). Instabilities in granular materials and application to landslides. *Mech. Cohesive-frictional Mater.* **5**, No. 8, 627–652.
- Darve, F., Servant, G., Laouafa, F. & Khoa, H. (2004). Failure in geomaterials: continuous and discrete analyses. *Comput. Methods Appl. Mech. Engng* **193**, No. 27–29, 3057–3085.
- Di, Y., Yang, J. & Sato, T. (2007). An operator-split ALE model for large deformation analysis of geomaterials. *Int. J. Numer. Analyt. Methods Geomech.* **31**, No. 12, 1375–1399.
- Donea, J., Giuliani, S. & Halleux, J. (1982). An arbitrary Lagrangian–Eulerian finite element method for transient dynamic fluid–structure interactions. *Comput. Methods Appl. Mech. Engng* **33**, No. 1–3, 689–723.
- Donea, J., Huerta, A. & Ponthot, J. (2004). Arbitrary Lagrangian–Eulerian methods. In *Encyclopedia of computational mechanics – volume 1 fundamentals* (eds E. Stein, R. de Borst and T. J. Hughes), Ch. 14, pp. 413–437. Chichester, UK: John Wiley & Sons, Ltd.
- Eichenberger, J., Nuth, M. & Laloui, L. (2013). Modeling landslides in partially saturated slopes subjected to rainfall infiltration. In *Mechanics of unsaturated geomaterials* (ed. L. Laloui), pp. 235–250. Hoboken, NJ, USA: John Wiley & Sons, Inc.
- François, B., Tacher, L., Bonnard, C., Laloui, L. & Triguero, V. (2007). Numerical modelling of the hydrogeological and geomechanical behaviour of a large slope movement: the Triesenberg landslide (Liechtenstein). *Can. Geotech. J.* **44**, No. 7, 840–857.
- Fredj, A. & Dinovitzer, A. (2010). Three-dimensional response of buried pipelines subjected to large soil deformation effects: part I – 3D continuum modeling using ALE and SPH formulations. In *Proceedings of 2010 8th international pipeline conference*, vol. 1, pp. 747–757. New York, NY, USA: American Society of Mechanical Engineers (ASME).
- Grant, D. (1996). *Instrumentation systems for and failure mechanisms of an induced slope failure project*. PhD thesis, University of Southampton, Southampton, UK.
- Guglielmi, Y. & Cappa, F. (2010). Regional-scale relief evolution and large landslides: insights from geomechanical analyses in the Tinée Valley (southern French Alps). *Geomorphology* **117**, No. 1–2, 121–129.
- Guilkey, J., Harman, T., Xia, A., Kashiwa, B. & McMurtry, P. (2003). An Eulerian–Lagrangian approach for large deformation fluid structure interaction problems, part I: algorithm development. In *Fluid structure interaction II: proceedings of the 2nd international conference on fluid structure interaction, Cadiz, Spain* (ed. S. K. Chakrabarti), pp. 143–156. Boston, MA, USA: WIT Press.



- Harlow, F. H. (1964). The particle-in-cell computing method for fluid dynamics. *Comput. Methods Physics* **3**, No. 3, 319–343.
- Harman, T., Guilkey, J. E., Kashiwa, B., Schmidt, J. & McMurtry, P. (2003). An Eulerian–Lagrangian approach for large deformation fluid structure interaction problems, part 2: multiphysics simulations within a modern computational framework. In *Fluid structure interaction II: proceedings of the 2nd international conference on fluid structure interaction, Cadiz, Spain* (ed. S. K. Chakrabarti), pp. 157–166. Boston, MA, USA: WIT Press.
- He, X. & Luo, L. S. (1997a). Theory of the lattice Boltzmann method: from the Boltzmann equation to the lattice Boltzmann equation. *Phys. Rev. E* **56**, No. 6, 6811–6121.
- He, X. & Luo, L. S. (1997b). A priori derivation of the lattice Boltzmann equation. *Phys. Rev. E* **55**, No. 6, R6333–R6336.
- Higo, Y., Oka, F., Kimoto, S., Morinaka, Y., Goto, Y. & Chen, Z. (2010). *A coupled MPM-FDM analysis method for multiphase elasto-plastic soils*. Tokyo, Japan: Japanese Geotechnical Society.
- Higo, Y., Nishimura, S. & Oka, F. (2015). Dynamic analysis of unsaturated embankment considering the seepage flow by a GIMPFD coupled method. In *Computer methods and recent advances in geomechanics* (eds F. Oka, A. Murakami, R. Uzuoka and S. Kimoto), pp. 1761–1766. London, UK: Taylor & Francis Group.
- Huang, P., Zhang, X., Ma, S. & Huang, X. (2011). Contact algorithms for the material point method in impact and penetration simulation. *Int. J. Numer. Methods Engng* **85**, No. 4, 498–517.
- Hungr, O., Evans, S., Bovis, M. J. & Hutchinson, J. N. (2001). A review of the classification of landslides of the flow type. *Environ. Engng Geosci.* **7**, No. 3, 221–238.
- Isono, H., Kohashi, H., Furumoto, K., Mori, H. & Ohno, M. (2004). Large model tests of levee reinforcement method with toe drain for seepage failure. In *Proceedings of annual symposium of Japanese Geotechnical Society*, pp. 1255–1256. Tokyo, Japan: Japanese Geotechnical Society (in Japanese).
- Jassim, I., Stolle, D. & Vermeer, P. A. (2013). Two-phase dynamic analysis by material point method. *Int. J. Numer. Analyt. Methods Geomech.* **37**, No. 15, 2502–2522.
- Jiang, J., Ehret, D., Xiang, W., Rohn, J., Huang, L., Yan, S. & Bi, R. (2010). Numerical simulation of Qiaotou landslide deformation caused by drawdown of the three Gorges reservoir, China. *Environ. Earth Sci.* **62**, No. 2, 411–419.
- Kafaji, I. (2013). *Formulation of a dynamic material point method (MPM) for geomechanical problems*. PhD thesis, University of Stuttgart, Stuttgart, Germany.
- Kardani, M., Nazem, M., Abbo, A. J., Sheng, D. & Sloan, S. W. (2011). Refined h-adaptive finite element procedure for large deformation geotechnical problems. *Comput. Mech.* **49**, No. 1, 21–33.
- Kim, H. & Inoue, J. (2007). A stochastic element free seepage flow analysis of heterogeneous subsurface. In *Numerical models in geomechanics NUMOG X* (eds G. Pande and S. Pietruszczak), pp. 225–231. London, UK: Taylor & Francis Group.
- Kumar, P. R., Dodagoudar, G. & Rao, B. (2008). Meshfree modeling of two-dimensional contaminant transport through unsaturated porous media. In *Unsaturated soils: advances in geo-engineering* (eds C. Augarde, D. Gallipoli and S. Wheeler), pp. 861–866. London, UK: Taylor & Francis Group.
- Kumar, K., Soga, K. & Delenne, J. Y. (2012). Granular flows in fluid. In *Discrete element modelling of particulate media* (ed. C. Y. Wu), Special Publication. Cambridge, UK: Royal Society of Chemistry.
- Lenti, L. & Martino, S. (2013). A parametric numerical study of the interaction between seismic waves and landslides for the evaluation of the susceptibility to seismically induced displacements. *Bull. Seismol. Soc. Am.* **103**, No. 1, 33–56.
- Li, S. & Liu, W. (2002). Meshfree and particle methods and their applications. *Appl. Mech. Rev.* **55**, No. 1, 1–34.
- Lu, Y., Belytschko, T. & Gu, L. (1994). A new implementation of the element free Galerkin method. *Comput. Methods Appl. Mech. Engng* **113**, No. 3–4, 397–414.
- Mackenzie-Helnwein, P., Arduino, P., Shin, W., Moore, J. A. & Miller, G. R. (2010). Modeling strategies for multiphase drag interactions using the material point method. *Int. J. Numer. Methods Engng* **83**, No. 3, 295–322.
- Maeda, K. & Sakai, H. (2010). Seepage failure and erosion of ground with air bubble dynamics. In *Geoenvironmental engineering and geotechnics: progress in modeling and applications* (eds Q. He and S.-L. Shen), pp. 261–266. Reston, VA, USA: American Society of Civil Engineers (ASCE).
- Mast, C. M., Arduino, P., Miller, G. R. & Mackenzie-Helnwein, P. (2014). Avalanche and landslide simulation using the material point method: flow dynamics and force interaction with structures. *Comput. Geosci.* **18**, No. 5, 817–830.
- Monaghan, J. (2005). Smoothed particle hydrodynamics. *Rep. Prog. Physics* **68**, No. 8, 1703–1759.
- Moresi, L., Dufour, F. & Mühlhaus, H. B. (2003). A Lagrangian integration point finite element method for large deformation modeling of viscoelastic geomaterials. *J. Comput. Physics* **184**, No. 2, 476–497.
- Mori, H. (2008). *The SPH method to simulate river levee failures*. MSc thesis, University of Cambridge, Cambridge, UK.
- Mueller, R. & Loew, S. (2009). Predisposition and cause of the catastrophic landslides of August 2005 in Brienz (Switzerland). *Swiss J. Geosci.* **102**, No. 2, 331–344.
- Nazem, M., Sheng, D., Carter, J. P. & Sloan, S. W. (2008). Arbitrary Lagrangian–Eulerian method for large-strain consolidation problems. *Int. J. Numer. Analyt. Methods Geomech.* **32**, No. 9, 1023–1050.
- Nazem, M., Carter, J. & Airey, D. (2009). Arbitrary Lagrangian–Eulerian method for dynamic analysis of geotechnical problems. *Comput. Geotech.* **36**, No. 4, 549–557.
- Nicot, F. & Darve, F. (2011). Diffuse and localized failure modes: two competing mechanisms. *Int. J. Numer. Analyt. Methods Geomech.* **35**, No. 5, 586–601.
- Oliver, J. & Huespe, A. (2004). Continuum approach to material failure in strong discontinuity settings. *Comput. Methods Appl. Mech. Engng* **193**, No. 30–32, 3195–3220.
- Oñate, E., Idelsohn, S. R., Celigueta, M. A. & Rossi, R. (2008). Advances in the particle finite element method for the analysis of fluid–multibody interaction and bed erosion in free surface flows. *Comput. Methods Appl. Mech. Engng* **197**, No. 19–20, 1777–1800.
- Oñate, E., Celigueta, M. A., Idelsohn, S. R., Salazar, F. & Suárez, B. (2011). Possibilities of the particle finite element method for fluid–soil–structure interaction problems. *Comput. Mech.* **48**, No. 3, 307–318.
- Pastor, M., Haddad, B., Sorbino, G., Cuomo, S. & Drempetic, V. (2009). A depth-integrated, coupled SPH model for flow-like landslides and related phenomena. *Int. J. Numer. Analyt. Methods Geomech.* **33**, No. 2, 143–172.
- Pastor, M., Blanc, T., Haddad, B., Petrone, S., Sanchez Morles, M., Drempetic, V., Issler, D., Crosta, G. B., Cascini, L., Sorbino, G. & Cuomo, S. (2014). Application of a SPH depth-integrated model to landslide run-out analysis. *Landslides* **11**, No. 5, 793–812.
- Prime, N., Dufour, F. & Darve, F. (2014). Solid-fluid transition modelling in geomaterials and application to a mudflow interacting with an obstacle. *Int. J. Numer. Analyt. Methods Geomech.* **38**, No. 13, 1341–1361.
- Qiu, G., Henke, S. & Grabe, J. (2011). Application of a coupled Eulerian–Lagrangian approach on geomechanical problems involving large deformations. *Comput. Geotech.* **38**, No. 1, 30–39.
- Ramos, A., Lizcano, A. & Andrade, J. (2012). Modelling diffuse instabilities in sands under drained conditions. *Géotechnique* **62**, No. 6, 471–478, <http://dx.doi.org/10.1680/geot.10.P109>.
- Rodriguez, M., Chamot-Rooke, N., Hébert, H., Fournier, M. & Huchon, P. (2013). Owen Ridge deep-water submarine landslides: implications for tsunami hazard along the Oman coast. *Nat. Hazards Earth Syst. Sci.* **13**, No. 2, 417–424.
- Rots, J., Nauta, P., Kuster, G. & Blaauwendraad, J. (1985). Smeared crack approach and fracture localization in concrete. *HERON* **30**, No. 1, 3–48.
- Sanavia, L. (2009). Numerical modelling of a slope stability test by means of porous media mechanics. *Engng Comput.* **26**, No. 3, 245–266.

- Shin, W. (2010). *Numerical simulation of landslides and debris flows using an enhanced material point method*. PhD thesis, University of Washington, Seattle, WA, USA.
- Shrestha, P. L., Shaller, P. J., Doroudian, M., Sykora, D. W. & Hamilton, D. L. (2011). The 2005 La Conchita landslide, California: part 2 – modeling. *Proceedings of international conference on debris-flow hazards mitigation: mechanics, prediction, and assessment*, Padua, Italy, pp. 751–758.
- Skempton, A. W. (1964). Long-term stability of clay slopes. *Géotechnique* **14**, No. 2, 77–102, <http://dx.doi.org/10.1680/geot.1964.14.2.77>.
- Steffen, M., Wallstedt, P., Guilkey, J., Kirby, R. & Berzins, M. (2008). Examination and analysis of implementation choices within the material point method. *Comput. Modeling Engng Sci.* **31**, No. 2, 107–127.
- Sulsky, D., Chen, Z. & Schreyer, H. (1994). A particle method for history-dependent materials. *Comput. Methods Appl. Mech. Engng* **118**, No. 1–2, 179–196.
- Sulsky, D., Zhou, S. J. & Schreyer, H. L. (1995). Application of a particle-in-cell method to solid mechanics. *Comput. Physics Commun.* **87**, No. 1–2, 236–252.
- Tsuji, T., Nakamura, K., Yabumoto, K. & Tanaka, T. (2007). Large-scale DEM-CFD coupling simulation. *J. Soc. Powder Technol., Japan* **44**, No. 3, 173–179.
- Xiong, Q., Madadi-Kandjani, E. & Lorenzini, G. (2014). A LBM–DEM solver for fast discrete particle simulation of particle–fluid flows. *Continuum Mech. Thermodynam.* **25**, No. 6, 907–917.
- Xu, L., Dai, F. C., Gong, Q. M., Tham, L. G. & Min, H. (2012). Irrigation-induced loess flow failure in Heifangtai Platform, North-West China. *Environ. Earth Sci.* **66**, No. 6, 1707–1713.
- Yerro, A., Alonson, E. & Pinyol, N. (2015). The material point method for unsaturated soils. *Géotechnique* **65**, No. 3, 201–217, <http://dx.doi.org/10.1680/geot.14.P.163>.
- Zabala, F. & Alonso, E. E. (2011). Progressive failure of Aznalcóllar dam using the material point method. *Géotechnique* **61**, No. 9, 795–808, <http://dx.doi.org/10.1680/geot.9.P.134>.
- Zhang, H. W., Wang, K. P. & Chen, Z. (2009). Material point method for dynamic analysis of saturated porous media under external contact/impact of solid bodies. *Comput. Methods Appl. Mech. Engng* **198**, No. 17–20, 1456–1472.
- Zhang, X., Krabbenhoft, K., Pedroso, D., Lyamin, A., Sheng, D., da Silva, M. V. & Wang, D. (2013). Particle finite element analysis of large deformation and granular flow problems. *Comput. Geotech.* **54**, 133–142.
- Zhang, X., Krabbenhoft, K., Sheng, D. & Li, W. (2015). Numerical simulation of a flow-like landslide using the particle finite element method. *Comput. Mech.* **55**, No. 1, 167–177.
- Zheng, Y., Gao, F., Zhang, H. W. & Lu, M. (2013). Improved convected particle domain interpolation method for couple dynamic analysis of fully saturated porous media involving large deformation. *Comput. Methods Appl. Mech. Engng* **257**, 50–163.
- Zienkiewicz, O. C., Shiomi, T. & Zienkiewicz, O. C. (1984). Dynamic behaviour of saturated porous media; the generalized Biot formulation and its numerical solution. *Int. J. Numer. Analyt. Methods Geomech.* **8**, No. 1, 71–96.